

Dark Matter Sees The Light

Patrick Meade, Michele Papucci and Tomer Volansky

*Institute for Advanced Study
Princeton, NJ 08540*

Abstract

We construct a Dark Matter (DM) annihilation module that can encompass the predictions from a wide array of models built to explain the recently reported PAMELA and ATIC/PPB-BETS excesses. We present a detailed analysis of the injection spectrums for DM annihilation and quantitatively demonstrate effects that have previously not been included from the particle physics perspective. With this module we demonstrate the parameter space that can account for the aforementioned excesses and be compatible with existing high energy gamma ray and neutrino experiments. However, we find that it is relatively generic to have some tension between the results of the HESS experiment and the ATIC/PPB-BETS experiments within the context of annihilating DM. We discuss ways to alleviate this tension and how upcoming experiments will be able to differentiate amongst the various possible explanations of the purported excesses.

1 Introduction

Recently there has been a series of experimental results suggesting that we may have indirectly detected dark matter (DM) within our Galaxy. The combination of the positron fraction measured by the PAMELA experiment [1] and the ATIC/PPB-BETS experiments [2,3], have led to a compelling picture of DM being responsible for a new population of positrons at high energies. These excesses, if confirmed, could in principle have alternative explanations through either refining our understanding of charged particle propagation within our Galaxy, or by identifying new astrophysical sources of positrons coming, for instance, from pulsars [4]. It is intriguing therefore, that new experimental data expected in the near future could not only confirm or contradict those results, but also allow us to possibly determine the physics behind these excesses. Furthermore, in the case of DM, such experiments could strongly constrain the various DM models.

Broadly speaking, the plethora of DM models bifurcate into either annihilating [5,6] or decaying [7] DM. In this paper we choose to focus on the former possibility as being the source of the electronic excesses. The above experiments then place strong restrictions on the models, so we adopt the following phenomenological inputs as constraints:

- There is an excess in the flux ratio $\Phi_{e^+}/\Phi_{e^++e^-}$ observed by the PAMELA experiment extending to *at least* 100 GeV [1].
- There is an excess in the ATIC/PPB-BETS experiments for the flux of charged electrons and positrons, $\Phi_{e^++e^-}$, extending to energies of ~ 700 GeV [2,3].
- There is no excess observed by the PAMELA experiment in the antiproton flux [8].
- In the absence of large local overdensity in the DM distribution (boost factor), the annihilation cross section in our galaxy needs to be $\mathcal{O}(100)$ times larger than a standard thermal WIMP.

These facts are not easily reconciled. The last of these assumptions follows from the large measured rates combined with the higher mass scale indicated by the ATIC/PPB-BETS anomaly. For the case of a WIMP DM, a large enhancement of the cross section is needed [9–11]. Alternatively, a large boost factor (BF) is required. However, such a possibility seems unlikely in light of the results from N-body simulations [12]. Furthermore, a model must prefer annihilation into leptonic final states so that the antiproton fraction is not overpopulated.

There has been a recent explosion in model building that attempts to incorporate the necessary ingredients to explain these excesses. Typically, these models explain the electronic activity by either assuming a symmetry that forbids hadronic production, or otherwise postulating an intermediate light state that can only decay into light leptons due to kinematics. Most of these studies have either stopped at the heuristic level of explanation, or attempted quantitatively only to postdict certain experiments. It is therefore desirable to consider a larger set of experimental data in order to better establish the correct model-building direction.

We attempt to address the following questions:

- Given a model that can explain the PAMELA and ATIC/PPB-BETS data, what are the experimental bounds arising from other experiments?
- What are the viable classes of models?
- For these models, what are the implications for upcoming experiments?

The most logical additional signature which has not been entirely explored is the one coming from photons. Whenever there are charged particles in the final state there will be additional photons radiated, leading to a model independent signature [13]. Additional sources of photons may contribute depending on the specific details of the model. Recently there have been a few papers [14–16] that have studied the bounds from high energy photons in models that explain the excesses. The authors of [15, 16] reached the conclusion that for most dark matter density profiles, experimental results rule out the possibility of annihilating DM as an explanation of the excesses. In [14, 15] the case where DM directly annihilates into a pair of SM leptons was studied. We reach a similar conclusion to [15], that such models disagree with the experimental data collected for high energy photons. In [16] models where DM annihilates through a light state and then into leptons was studied. In our paper we focus on these models and reach a different conclusion than the authors of [16]. While we find there exists some tension between models that explain ATIC/PPB-BETS and high energy photons, they are not ruled out by an order of magnitude. We also include several effects that have not yet been studied in the literature, that can ameliorate this tension, such as dark sector radiation.

To study the implications of the present experimental data, we construct a module that incorporates many of the required features necessary for a model to explain the excesses. This module has several parameters that allow us to interpolate between different classes of models.

Our main results are summarized as follows. For annihilating DM scenarios that explain both PAMELA and ATIC/PPB-BETS:

- Rather generically, such models are in tension with constraints from high-energy photons.
- Photons are more constraining than the antiprotons measurements. In particular, models that produce antiprotons and still fit the PAMELA data in many cases produce too many photons to be consistent with the measurements.
- The tension is not sufficient to exclude all models. However, it requires a factor of order $\mathcal{O}(2 - 5)$ that may arise from various sources, e.g. a local boost factor or a less cuspy DM profile.

We find a number of interesting implications based on these results. Upcoming experiments have the power to exclude the full region of parameter space, for models that explain the ATIC/PPB-BETS excesses with annihilating DM. From this point of view decaying DM

models are attractive because they generate fewer photons at the center of the galaxy. Models of annihilating DM that do not seek to explain the ATIC/PPB-BETS are also viable, and can be tested with several ongoing experiments. In particular, we stress the importance of the currently running experiment, FERMI [17], for helping determine the underlying nature of these excesses.

This paper is organized as follows. In Section 2 we construct a DM module that enables us to investigate the parameter space of models. We then calculate the particle physics input for the relevant experiments, namely the injection spectrums for e^+ , \bar{p} , γ and ν . In Section 3 we discuss the astrophysical inputs for our study. We review the methods used in this study for propagating the various particles from their source to Earth. Additionally, we further discuss the experimental inputs that we use, and comment on many of the uncertainties associated in calculating the fluxes for them. In Section 4 we present the resulting astrophysical fluxes calculated from our particle physics module. We demonstrate how the various particle physics and astrophysics parameters affect the predicted fluxes for e^+ , \bar{p} , γ and ν . Finally, in Section 5 we discuss the implications and interpretations of the regions of parameter space that we find to be consistent with the experiments studied. In Appendix A we discuss the so called “leaky box” approximation which we use to estimate the positron background flux.

2 Unified Dark Matter Module

We are interested in understanding the bounds and predictions for characteristic DM models that could be used to explain the excesses observed. In this work we do not focus on the bounds for a particular model nor are we completely model independent. Instead, we construct a module that contains the most important components that we identify from the particle physics perspective. This module can then be appropriately recast to reflect the predictions from a wide array of models that have been, and inevitably will be, built.

We construct the dark matter module loosely in accord with the Unified Dark Matter model of Arkani-Hamed *et al.* [5]. This model offers the intriguing possibility to describe not only the PAMELA and ATIC/PPB-BETS excesses, but also the INTEGRAL [18] and DAMA [19] excesses simultaneously. We treat [5] as representative of a class of ideas, and choose to incorporate those features of [5] that are relevant to studying the experimental consequences for indirect searches in the high energy e^+ , \bar{p} and γ channels.

The components we choose to include in our module for explaining the excesses are the following. We assume there are heavy DM particle(s), $\chi(s)$, that are charged under some “dark” gauge group, and possibly the SM electroweak (EW) gauge groups as well. Additionally, the dark gauge group is broken and therefore the sector consists of light gauge bosons which we collectively refer to as ϕ . The light gauge bosons are required for two reasons: On the one hand, they allow for a kinematical explanation for the electron but no antiproton excess measured by the above experiments. On the other hand, they play part in the Sommerfeld mechanism that can enhance the usual thermal WIMP cross-section to the required rate today. With this in mind, we allow the χ ’s to annihilate either through

the SM EW gauge bosons, $V = (W, Z)$, or the ϕ 's:

$$\chi\chi \rightarrow VV \text{ or } \chi\chi \rightarrow \phi\phi. \quad (2.1)$$

If χ annihilates through SM gauge bosons, then the final states are clear. The annihilation into ϕ needs further explanation. If one assumes that there are measurable consequences in experiments then ϕ ultimately needs to decay into SM final states. There are two possibilities that allow ϕ to decay. Either the SM matter fields are charged under the dark gauge group, in which case ϕ can decay into SM fields based on their charge assignments. Otherwise, the ϕ gauge bosons can mix with the SM gauge bosons and thereby decay through this mixing. While either scenario is possible in principle, we will choose the latter and couple ϕ to the SM matter through gauge boson mixing. On general grounds the vector ϕ will decay back to SM states by mixing through the photon or the Z boson. However, given the lightness of ϕ , the decays going through Z mixing will be further suppressed by at least m_ϕ^2/m_Z^2 . Unless the γ - ϕ mixing is much smaller than the Z- ϕ mixing, one can then assume that ϕ couples to SM particles proportionally to their electric charge. Hence the ϕ decay branching fractions are completely determined by its mass. An example annihilation is shown in Figure 1.

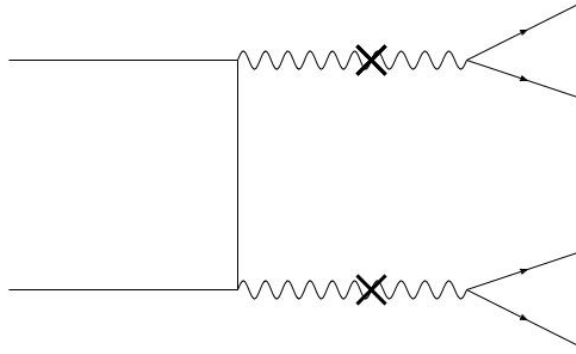


Figure 1: An example of χ annihilation, $\chi\chi \rightarrow \phi\phi \rightarrow e^+e^-e^+e^-$ via the mixing of ϕ and γ .

With these considerations we have come up with a minimal module that has five particle physics parameters:

- m_χ - sets the mass scale for the DM annihilation.
- m_ϕ - determines what states ϕ can decay into and the kinematics of the decay products.
- α_{DM} - the strength of the gauge coupling in the dark sector.
- $\langle\sigma v\rangle \equiv \langle\sigma v\rangle_{VV} + \langle\sigma v\rangle_{\phi\phi}$ - a free parameter for the overall cross section.
- $R_{\text{SM}} = \frac{\langle\sigma v\rangle_{VV}}{\langle\sigma v\rangle}$ - a free parameter for the relative contributions of the annihilations into the SM vs dark gauge bosons.

While some of these parameters may seem redundant, they allow us to cover the parameter space of a large number of models without having to calculate within each model separately. In particular, the inclusion of α_{DM} as a separate parameter is noticeable as we keep $\langle\sigma v\rangle$ and R_{SM} free.

Once we stipulate that ϕ is a dark gauge boson, we need to allow for the possibility that the dark gauge group is nonabelian. In fact this is exactly what is desired in [5] to explain DAMA and INTEGRAL anomalies. If ϕ represents collectively the gauge bosons of a nonabelian group, then there are additional processes for annihilation into the SM compared to those shown in Figure 1. Just like in QCD once the gauge bosons are produced,

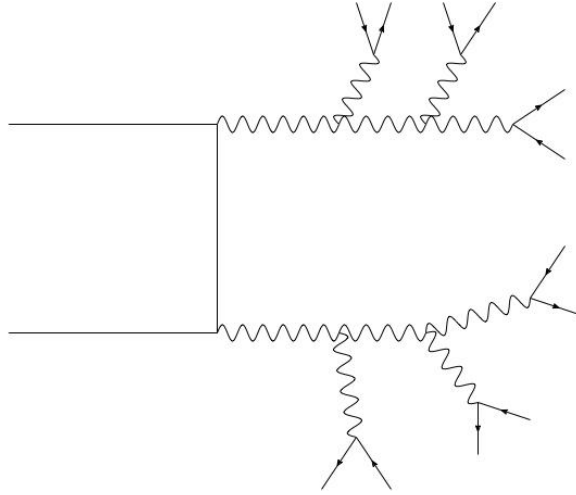


Figure 2: An example of $\chi\chi$ annihilation, with the inclusion of the dark sector shower.

they can shower and split into new gauge bosons. We give an example of this process in Figure 2, where after showering the dark gauge boson subsequently decays into SM final states through photon mixing. This process has not been quantitatively explored before in this context and we demonstrate the effect in later sections. As we shall see, while naively there is no large enhancement as the ϕ 's are massive, a significant change in the resulting energy spectrum arises since we assume $m_\chi \gg m_\phi$.

There additionally could be another annihilation channel for χ , i.e. $\chi\chi \rightarrow Z\phi$. This is strongly dependent on the model, and could in principle be used as a separate parameter in our module. For instance this mode will not occur with any appreciable rate in models where χ is a single Majorana particle. We choose not to include this as a separate parameter, and instead one can infer bounds on this mode from our R_{SM} appropriately rescaled.

2.1 Calculation of Injection Spectrum

In this section we calculate the particle physics input for all dark matter indirect experiments. For the experiments that we are interested in, we simply need the injection spectrum of e^+ , \bar{p} , γ , and ν coming from the annihilation of the χ 's. Therefore we need to calculate the inclusive

annihilation of $\chi\chi$ at threshold and then extract the energy distribution, dN/dE , for each particle we are interested in.

To calculate dN/dE we implement our module in several MC programs and scan over the particle physics parameters m_χ, m_ϕ and α_{DM} that define it. We do *not* calculate $\langle\sigma v\rangle$ and R_{SM} from first principles, instead we will *fit* the experimental data for PAMELA and ATIC/PPB-BETS to fix these parameters. The result of this fit will then dictate what boost factor is needed compared to a standard thermal WIMP annihilation cross section. If one calculated the Sommerfeld effect within a model, this would constrain the values of the masses and gauge couplings given the necessary cross section. However, since we do not wish to focus on one particular model alone, we do not require this consistency check. Additionally once the mass and α_{DM} are given, a model could predict the ratio R_{SM} . However, R_{SM} can also be an independent of α_{DM} , for instance if the DM fields χ are singlets under the SM and mixed through a Yukawa coupling.

To implement the module in event generators we make the specific choice of $SU(2)$ for the dark gauge group, and we define χ to be a bi-doublet under the SM $SU(2)$ and the hidden $SU(2)$. This choice *only* affects the dark gauge boson parton shower directly, since $\langle\sigma v\rangle$ and R_{SM} are fit to data. However, since we will scan over α_{DM} , a different choice of coupling can still be used to approximately interpolate amongst different Casimirs and extrapolate the results to different gauge groups.

The parameter space we choose to cover is shown in Table 1. Our choice of whether to implement a parton shower in the dark sector is a binary one. This allows us to cover the case where the dark gauge group is $U(1)$ and the gauge bosons don't shower.

No dark sector parton shower	
m_χ	200 GeV - 3.5 TeV
m_ϕ	200 MeV, 500 MeV, 1.2 GeV, 8 GeV, 15 GeV
α_{DM}	arbitrary
Dark sector parton shower	
m_χ	200 GeV - 3.5 TeV (discrete grid)
m_ϕ	200 MeV, 500 MeV, 1.2 GeV, 8 GeV, 15 GeV
α_{DM}	$10^{-3}, 10^{-2}, 4 \cdot 10^{-2}, 10^{-1}$

Table 1: Parameters scanned in the DM module.

To implement the decays of the ϕ particle we use different effective field theories depending on the mass of ϕ that we are interested in. When $m_\phi \gg \Lambda_{QCD}$, we coupled ϕ directly to the quarks at parton level, which can then be showered and hadronized. On the other hand if $m_\phi \lesssim$ a few GeV, this procedure is a bad approximation. In this case we couple ϕ directly to mesons. We take the corresponding cross sections from experimental data of $e^+e^- \rightarrow \text{hadrons}$ exclusive processes [20]. In particular for the 500 MeV case, we assume ϕ decays to e^+e^- , $\mu^+\mu^-$, $\pi^+\pi^-$ and the ratio is approximately 2:2:1 as shown in Table 2. For the 1.2 GeV case we include other mesonic 2-body modes as well as 3- and 4-body decays that are non-negligible. We did not implement any other intermediate mass between 1.2 GeV

and 8 GeV because multi-body final states become increasingly important and there is not enough experimental information to completely reconstruct the exclusive final states. The 8 GeV and 15 GeV were chosen to have m_ϕ separated enough from the quarkonia resonance region (where the hadronization model we use from Pythia [21] suffers from large uncertainties) and be above and below the $b\bar{b}$ threshold. We catalogue the decay modes implemented and branching fractions of ϕ in Table 2.

m_ϕ	Mode	BF
200 MeV	$\phi \rightarrow e^+e^-$	1
500 MeV	$\phi \rightarrow e^+e^-$	$4 \cdot 10^{-1}$
	$\phi \rightarrow \mu^+\mu^-$	$4 \cdot 10^{-1}$
	$\phi \rightarrow \pi^+\pi^-$	$2 \cdot 10^{-1}$
1.2 GeV	$\phi \rightarrow e^+e^-$	$3.4 \cdot 10^{-1}$
	$\phi \rightarrow \mu^+\mu^-$	$3.3 \cdot 10^{-1}$
	$\phi \rightarrow \omega\pi^0$	$7.9 \cdot 10^{-2}$
	$\phi \rightarrow \pi^+\pi^-\pi^0\pi^0$	$7.5 \cdot 10^{-2}$
	$\phi \rightarrow \pi^+\pi^-$	$6.4 \cdot 10^{-2}$
	$\phi \rightarrow K^+K^-$	$4.5 \cdot 10^{-2}$
	$\phi \rightarrow \pi^+\pi^+\pi^-\pi^-$	$4.1 \cdot 10^{-2}$
	$\phi \rightarrow \pi^+\pi^-\pi^0$	$2.4 \cdot 10^{-2}$
	$\phi \rightarrow K^0\bar{K}^0$	$5 \cdot 10^{-3}$
m_ϕ	Mode	BF
8 GeV	$\phi^+ \rightarrow e^+e^-$	$1.6 \cdot 10^{-1}$
	$\phi \rightarrow \mu^+\mu^-$	$1.6 \cdot 10^{-1}$
	$\phi \rightarrow \tau^+\tau^-$	$1.6 \cdot 10^{-1}$
	$\phi \rightarrow u\bar{u}$	$2.1 \cdot 10^{-1}$
	$\phi \rightarrow d\bar{d}$	$5.2 \cdot 10^{-2}$
	$\phi \rightarrow c\bar{c}$	$2.1 \cdot 10^{-1}$
	$\phi \rightarrow s\bar{s}$	$5.2 \cdot 10^{-2}$
15 GeV	$\phi^+ \rightarrow e^+e^-$	$1.5 \cdot 10^{-1}$
	$\phi \rightarrow \mu^+\mu^-$	$1.5 \cdot 10^{-1}$
	$\phi \rightarrow \tau^+\tau^-$	$1.5 \cdot 10^{-1}$
	$\phi \rightarrow u\bar{u}$	$2.0 \cdot 10^{-1}$
	$\phi \rightarrow d\bar{d}$	$5.0 \cdot 10^{-2}$
	$\phi \rightarrow c\bar{c}$	$2.0 \cdot 10^{-1}$
	$\phi \rightarrow s\bar{s}$	$5.0 \cdot 10^{-2}$
	$\phi \rightarrow b\bar{b}$	$4.8 \cdot 10^{-2}$

Table 2: Branching Fractions for ϕ . The values for 0.5 and 1.2 GeV are extracted from experimental data for exclusive $e^+ + e^- \rightarrow \text{hadrons}$ processes [20], while for 8 and 15 GeV are computed using BRIDGE.

To calculate the injection spectrums using existing Monte Carlo (MC) tools is quite difficult. The kinematic regime we study is based on very heavy particles annihilating through very light particles, that subsequently decay. In this regime most MC generators that we have used have difficulties. To generate our injection spectrums we were forced to use a variety of generators linked together depending on the task: MadGraph/MadEvent [22], BRIDGE [23], SHERPA [24], and Pythia [21].

For the SM annihilations $\chi\chi \rightarrow VV \rightarrow \text{fermions}$, we generate parton level events keeping spin correlations. We then shower and hadronize, including the effects of photons that are showered from the W gauge bosons [25]. To generate $\chi\chi \rightarrow \phi\phi \rightarrow SM$ without the dark sector parton shower we again generate parton level events including spin correlations. We then shower and hadronize either the fundamental particles, or just shower the charged mesons and their decay products. Unlike [16], when applicable, we include the $\mathcal{O}(1)$ effects of calculating photons showered from muon decays.

For the case when we include the dark sector parton shower, we first need to calculate the massive vector boson splitting function for the $SU(2)$ case that we have implemented. Given

the kinematics that we scan over, $m_\chi \gg m_\phi$, the effects of the massive splitting function are minor and it is sufficient to use the massless splitting functions,

$$P_{\phi \rightarrow \phi\phi}(z) = \frac{\alpha_{\text{DM}}}{2\pi} \frac{2(1-z(1-z))^2}{z(1-z)}. \quad (2.2)$$

Nevertheless in our computation we include the complete massive splitting function which only differs by the inclusion of another term that is subdominant over most of our kinematic range. To generate events including the dark sector parton shower, we compute the $2 \rightarrow 2$ matrix element. We then shower in the dark sector and decay the ϕ keeping some of the spin correlations. Finally, we shower and hadronize the SM particles that come from the ϕ decays, including the effects listed previously.

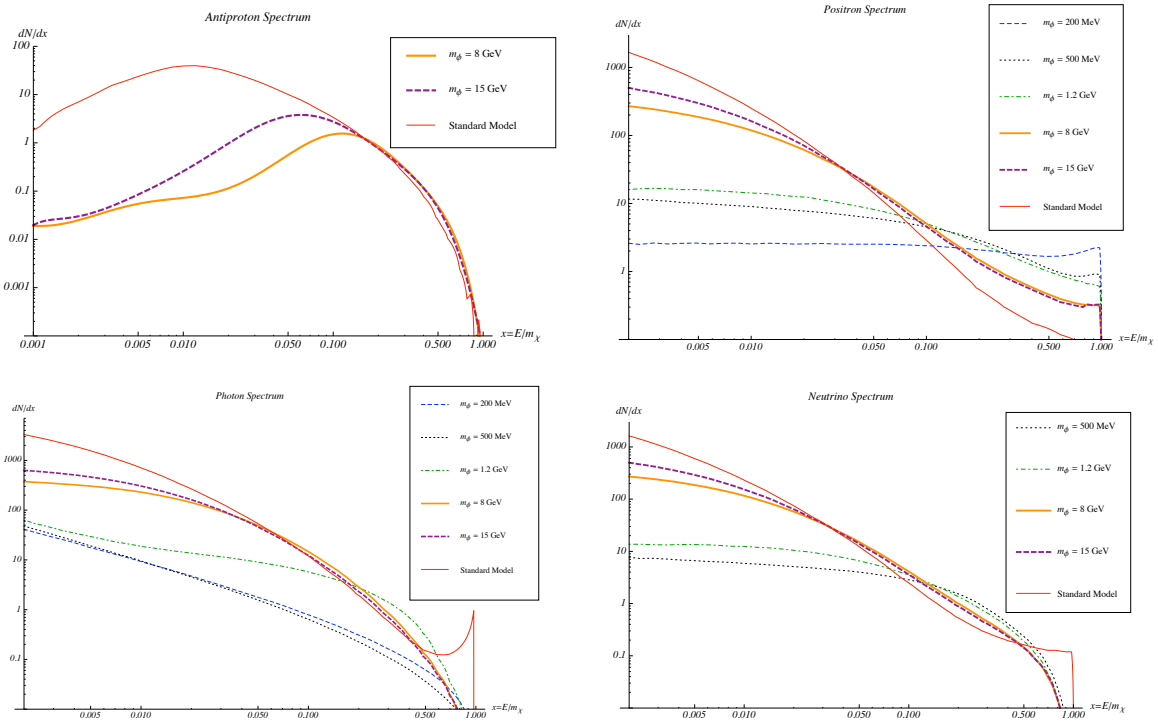


Figure 3: dN/dx for \bar{p}, e^+, γ , and ν for the various m_ϕ used. The SM contribution from $\chi\chi \rightarrow VV$ is also shown. In the range of x plotted we never reach Λ_{QCD}/m_χ thus the shapes are universal and independent of m_χ , even for the antiprotons.

In Figure 3 we plot dN/dx , where $x = E/m_\chi$, for \bar{p}, e^+, γ , and ν for different m_ϕ with no parton shower included. We additionally include the SM annihilation channel $\chi\chi \rightarrow VV$. For later reference, we also plot in Figure 4 the photon and positron spectrum for the two body decay $\chi\chi \rightarrow e^+e^-$. Both the SM annihilation channels will be used below for comparison with different models and to study the constraints on annihilating through the SM gauge bosons. As one can see, the larger the number of open decay channels for ϕ , the larger the population of low energy particles, namely the softer the spectrum. One can see that in

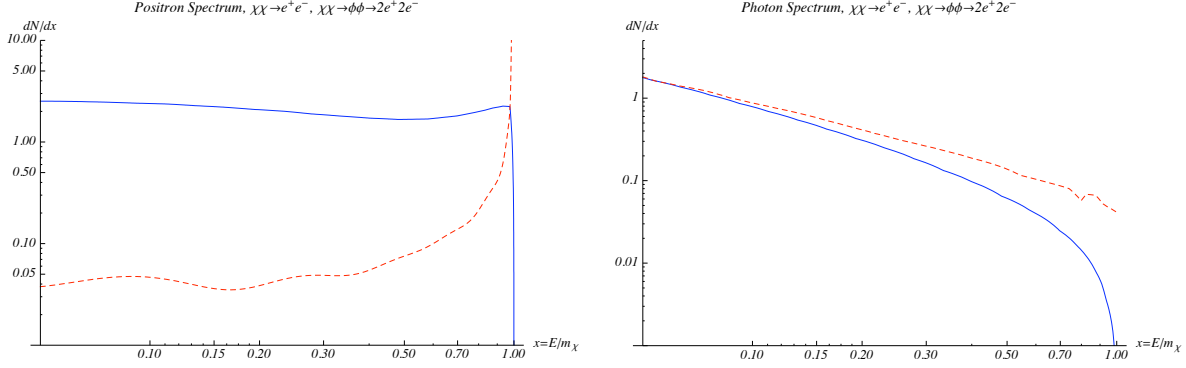


Figure 4: Photon and positron spectrum for the two body decay $\chi\chi \rightarrow e^+e^-$ (dashed red line). For comparison, we also plot the four body decay $\chi\chi \rightarrow 2\phi \rightarrow 2e^+2e^-$ (solid blue line).

the 8 GeV, 15 GeV and SM gauge boson cases, showering and hadronization effects from QCD induce several orders of magnitude increase in dN/dx . Moreover, showering effects also softens the spectrum of the direct decay into e^+e^- , as is clear from Figure 4.

In Figure 5 we plot dN/dx , for \bar{p}, e^+, γ , and ν for different values of α_{DM} to illustrate the effects of the dark sector parton shower. Without showering, the spectrum, dN/dx , is universal and independent of m_χ , this is no longer true when showering is taken into account. The reason for this is that the number of energy decades for showering depends on the ratio m_χ/m_ϕ . Hence in order to demonstrate the α_{DM} dependence, we fix the value of m_χ and m_ϕ . One should note that showering can have a large effect on the dN/dx . Hidden sector showering not only softens the spectrum via radiation, but also through additional ϕ decays.

2.1.1 Particle Physics Uncertainties

In this section we review some of the uncertainties in calculating the dN/dE for e^+ , \bar{p} , ν and γ . Most channels are rather clean from the particle physics perspective, but there are several issues that can have a significant effect on the dN/dx that we compute. These issues are hadronic uncertainties in the calculation of the dN/dx for \bar{p} , showering uncertainties which change the photon spectrum and the effects associated with the possibility of having different matrix elements which can affect all particles.

Hadronic uncertainties are due to the fact that once we have SM quarks we need to turn these partons into mesons and baryons through hadronization/fragmentation. While QCD can correctly describe the parton showering evolution, the process of hadronization relies upon phenomenological models that are tuned to data. While the effects of hadronization are important in some specific collider searches, when discussing high energy jets at colliders, one rarely talks about exclusive channels that label specific numbers of mesons and baryons. On the other hand, in the case of DM we look at the fully exclusive \bar{p} channel. To hadronize we use the Pythia program. Pythia employs several possible fragmentation models for creating baryons such as diquark, popcorn and advanced popcorn. The Pythia manual [21], states

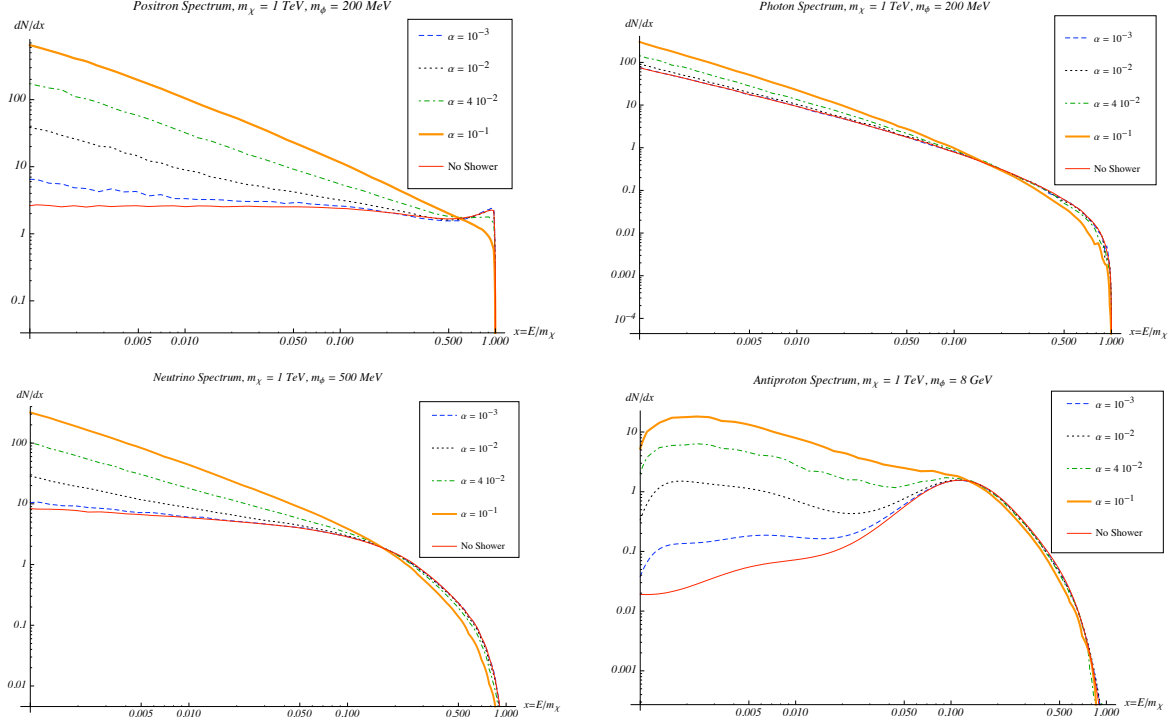


Figure 5: The effect of varying α_{DM} over the range given in Table 1. We plot dN/dx for a given particle type with a fixed $m_\chi = 1$ TeV and various m_ϕ .

that the tuning of their baryon production models are done with a global fit to the data and that the resulting fragmentation functions for individual baryons can be lower or higher than the actual data. To quantify this effect we used the Pythia default popcorn algorithm, and compare it with the advanced popcorn algorithm and SHERPA's AHADIC++ algorithm. We find that there is an $\mathcal{O}(1)$ effect in using different hadronization/fragmentation algorithms for the \bar{p} injection spectrum.

For showering, there are various levels of sophistication that one may try to employ. For instance in comparison with [16] we include the effects of showering off the decay products of the muon while they only include the shower from the muon itself. We find that this is an $\mathcal{O}(1)$ effect over the entire range of energies that we examine. Additionally there are further uncertainties depending on how the parton shower is implemented. For instance, when SHERPA is used to compute the radiative decays of the vector ϕ , taking into account the full matrix element structure for $l^+l^-\gamma$, it tends to underpopulate the high energy gammas compared to the parton shower approximation. Since the above effect is model dependent, we do not consider it here and instead, rely solely on the parton shower. Nevertheless, one should keep in mind that this discrepancy induces another $\mathcal{O}(1)$ effect that may reduce or enhance our results.

As in the case of ϕ decays, differences between matrix elements can introduce a nontrivial dN/dx shape dependence which translates into different fluxes observed in experiments. This

has been studied in the literature e.g. [26]. Including non trivial effects of spin correlation, typically do not introduce large changes in the positron spectrum [26], since usually the spectrum changes only at very high energy. However, depending on the form of the positron injection spectrum, this can lead to non trivial changes in the region of interest for gamma ray searches. While we only take the matrix element for $2 \rightarrow 4$ assuming there is an intermediate light gauge boson, one should keep in mind that there could be a factor of a few uncertainty if the underlying model was different.

3 Astrophysics Inputs

In this section we review the astrophysical propagation of e^+ , \bar{p} , ν and γ . Due to a lack of theoretical understanding and experimental data, propagation models suffer from large uncertainties and there are various models that exist in the literature. The choice of a model is not only important for estimating the DM signal, but also for correctly evaluating the backgrounds. Using different models may result in significantly different predictions.

As an example, we could, in principle, use a program such as GALPROP [27] and calculate both the background and signal propagation by using a best fit propagation model. However, we aim to be as data driven as possible and introduce the minimal amount of theory necessary to estimate both the signal and background. We therefore use semi-analytical propagation method which we review below. This approach has been studied extensively in the literature [28, 29] and it therefore allows for a simple estimation of the underlying uncertainties. In later sections we will briefly revisit some of these uncertainties.

We can also employ a data-driven analytic approach to estimate the backgrounds. Whenever we can, we use known measurements or otherwise conservative models for the evaluation of the backgrounds. Below we discuss the propagation model, the experimental data and the background estimation for each of the relevant channels. We discuss in each case the uncertainties involved and explain how we take those into account when fitting the predictions to the data.

3.1 DM Halos

In this section we review the DM density profiles that we use as inputs when calculating the fluxes from DM annihilation. Most of the dark matter profiles that we consider here are inferred from N-body simulations. Starting in the mid-nineties, a paradigm emerged [30] where by examining the results of dark matter N-body simulations for many different galaxies, a type of universality for the density profiles appeared. This led to the famous NFW profile [30] for dark matter that is in common use today. Since then other groups have examined this universality and found similar results. Nevertheless, there is some disagreement between groups concerning how cuspy the dark matter profile is at the center of the galaxy. Most standard dark matter profiles can be parameterized using the (α, β, γ) parametrization [31]

$$\rho(r) = \rho_{\odot} \left[\frac{r_{\odot}}{r} \right]^{\gamma} \left[\frac{1 + (r_{\odot}/r_s)^{\alpha}}{1 + (r/r_s)^{\alpha}} \right]^{(\beta-\gamma)/\alpha}. \quad (3.1)$$

The two most commonly used profiles of this type are NFW [30] and Moore [32]⁽¹⁾. Additionally the Isothermal profile [34] also fits into this parameterization, but it is based on older approximations for dark matter halos and there is no evidence for it in N-body simulations. While we do not consider the Isothermal profile viable, we show it below for the sake of comparison. In (3.2) we list the values of $(\alpha, \beta, \gamma, r_s)$ that correspond to the commonly used profiles.

ProfileName	α	β	γ	$r_s(\text{kpc})$
NFW	1	3	1	20
Moore	1	3	1.16	30
Isothermal	2	2	0	5

(3.2)

Recently N-body simulations have been able to increase their resolution by using $\mathcal{O}(10^9)$ particle simulations. From this, one is able to test the validity of the commonly used profiles such as NFW. It turns out that, as the resolution has increased and one has been able to probe further and further in towards the center of the Galaxy, the cusiness does not persist. This has led [35] to propose that, instead of the commonly used profiles in (3.2), the best fit profile is the so called Einasto profile [36]⁽²⁾:

$$\rho(r) = \rho_\odot \exp \left[\frac{-2}{\alpha} \left(\left(\frac{r}{r_s} \right)^\alpha - 1 \right) \right]. \quad (3.3)$$

What determines the deviation from the power law behavior is the Einasto α parameter which was found in [35] to have a mean value of 0.172 when fitting to simulations based on a few hundred million particles carried out by the Virgo consortium. Recently billion particle simulations have been carried out. The Aquarius [38], Via Lactea [39], and GHALO [40] simulations all fit the Einasto profile and α has been found to lie in the range $[0.142, 0.177]$. To be conservative, we choose a larger range of α consistent with [35]. Below, we will examine $\alpha = 0.12, 0.17, 0.20$.

The cusiness of the profile is not the only important feature, the local density is obviously crucial as well. Unfortunately our local density can not be pinned down very well from N-body considerations alone since the simulations do not include baryons. The value of the local density used in most dark matter detection studies is $\rho_\odot \simeq 0.3 \text{ GeV/cm}^3$ [41, 42], however this is based upon an older understanding of potential DM density profiles. A more recent study that has attempted to fix this value more carefully and construct a probability distribution for ρ_\odot , finds a canonical value of $\rho_\odot \simeq 0.4 \text{ GeV/cm}^3$ that can vary by up to a factor of ~ 10 , but is likely to be less not more than a factor of 2 [43]. While the N-body simulations can not constrain this value very well, the recent study based on the *Via Lactea II* billion particle simulation finds a value consistent with this, albeit with a possible large

⁽¹⁾The Moore profile has been attributed to several values of α, β, γ . The original profile, often referred to as M99, is very cuspy and has $\gamma = 1.5$. Sometimes this is used in dark matter calculations and it artificially inflates the rate of annihilations in the center of the Galaxy. While there is no longer evidence for this cuspy of profile, a more modern study by Moore *et al.* [33] found a best fit with $\gamma = 1.2$ which is usually denoted as Moore2004.

⁽²⁾This is sometimes referred to as a Merritt profile in the literature [37].

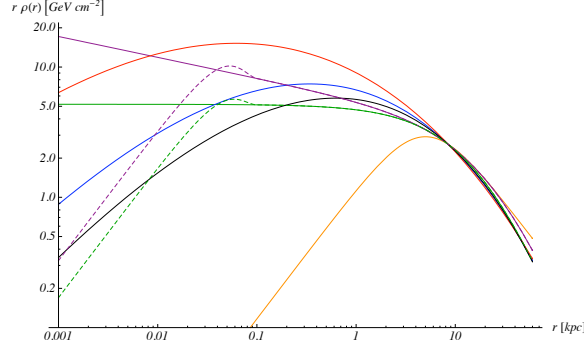


Figure 6: $r\rho(r)$ for the different DM profiles. When appropriate, we also plot the regularized profile, with $r_c = 100$ pc. Thick lines (from the bottom up): Einasto profile with $\alpha = 0.2, 0.17, 0.12$. Thin lines: isothermal, NFW, Moore (2004). The dashed lines represent the effect of the regularization described in the text.

variation due to local clumping of dark matter in their simulation [44]. For our purposes we will use a value of $\rho_\odot \simeq 0.3$ GeV/cm³ so our results can be easily compared with those of other groups. Nonetheless, but one should keep in mind this potential uncertainty when examining our results.

Finally, the cuspy profiles which diverge as $r \rightarrow 0$, should be regularized. Similar to [45], we regularize the NFW [30] and Moore [32] profiles, by assuming at small $r < r_c = 100$ pc, the DM density takes the form

$$\frac{\rho(r < r_c)}{\rho(r_c)} = A_1 + A_2 \operatorname{sinc}\left(\frac{\pi r}{r_c}\right) + A_3 \operatorname{sinc}^2\left(\frac{\pi r}{r_c}\right). \quad (3.4)$$

The coefficients A_i are determined by demanding that $\rho(r)$ and its first derivative are continuous and that the regularization does not alter the overall DM mass in the Galaxy. As we show later, the DM signal is rather sensitive to r_c .

In Figure 6 we plot the various DM profiles as a function of the radial distance from the Galactic center (GC). When appropriate, we also show the regularized profile.

3.2 Positrons

3.2.1 Propagation

To calculate the positron flux at the Earth one needs to understand how positrons propagate through our Galaxy. Due to our limited understanding of the latter, we wish to use a simplified model which employs a minimal set of assumptions. Perhaps the simplest model is the so called leaky box model which assumes a free homogeneous diffusion of charged particles within the Galactic disk. Since in its simplest form the model does not take particle cooling into account and since DM is not homogeneously distributed in the Galaxy, it is insufficient for calculating the DM signal. However, it is useful for calculating backgrounds and we will return to this model in Section 3.2.2 and the Appendix.

Below we adopt a widely studied diffusion model which does take cooling into account. Ignoring other effects in the propagation (such as convection and re-acceleration) is consistent for positrons at energies above ~ 10 GeV [28]. Moreover, the popularity of this model among the DM community allows one to compare our results with those of others, thereby emphasizing the new particle-physics features of our study. Where appropriate, we will remark on the uncertainties both in our theoretical understanding of the physical mechanisms involved and in the experimental tuning of the model [29].

To this end, the diffusion-loss equation in the steady state regime takes the form [46, 47]

$$-K(E)\nabla^2 n_{e^+}(E, x) - \frac{\partial}{\partial E} (b(E)n_{e^+}(E, x)) = Q_{e^+}(E, x). \quad (3.5)$$

Here $n_{e^+}(E, x)$ is the positron number density per unit energy which is related to the positron flux through $\Phi_{e^+} = v_{e^+} n_{e^+} / 4\pi$. $Q_{e^+}(E, x)$ is the source term for the positrons which for the background will be discussed in section 3.2.2 while for the DM source is given by

$$Q_{e^+}(E, r) = \frac{1}{2} \frac{\rho(r)^2}{M_{\text{DM}}^2} \sum_k \langle \sigma v \rangle_k \frac{dN_{e^+}^k}{dE}. \quad (3.6)$$

Finally

$$b(E) = \frac{E^2}{\text{GeV } \tau_E}, \quad (3.7)$$

is the energy loss coefficient due to Inverse Compton Scattering (ICS) and Synchrotron Radiation, with $\tau_E = 10^{16}$ s. Here and below, E denotes the kinetic energy of the corresponding particle. The diffusive region is assumed to be a flat cylinder parameterized by (r, z, θ) , with $z \in [-L, L]$ and $r \in [0, R]$, $R = 20$ kpc. The positron number density is taken to vanish at the boundaries and particles may propagate freely outside of it. The solar system is located at $(r_\odot, z_\odot, \theta_\odot) = (8.5 \text{ kpc}, 0, 0)$.

Diffusion arises due to the interactions of charged particles with the galactic magnetic field inhomogeneities. Such interactions produce stable and unstable spallation products that may be used to extract the height of the diffusion region, L , and the diffusion coefficient $K(E)$ which is usually taken to be of the form

$$K(E) = K_0 \beta (\mathcal{R}/\text{GV})^\delta. \quad (3.8)$$

Here $\beta = v/c$ and $\mathcal{R} = pc/eZ$ is the rigidity of the particle. For electrons and positrons, $e\mathcal{R} \simeq E$. The most stringent constraint on the above parameters comes from the B/C measurements of the HEAO-3 experiment [48] and other balloon experiments, the most recent being ATIC-2 [49]. The range for K_0 , δ and L has been studied e.g. in [27, 50]. We adopt the parameters of [51], shown in Table 3. The (MIN, MAX) are taken to extremize the antiproton flux, while the (M1, M2) extremize the positron flux. However, as it will be shown below, the differences between MIN and M2 are small for the positrons, while MIN encompasses a larger spread for the antiprotons. These sets of parameters are used as representatives of the uncertainties in the diffusion model. It is important however to

Model	δ	K_0 [kpc ² /Myr]	L [kpc]	V_C [km/s]
MIN	0.85	0.0016	1	13.5
MED	0.70	0.0112	4	12
MAX (M1)	0.46	0.0765	15	5
M2	0.55	0.00595	1	8

Table 3: Parameters for the cosmic ray propagation model, compatible with measurements of B/C. The names correspond to minimum, medium or maximum primary antiproton and positron fluxes. The convective wind parameter V_C is only relevant to the propagation of antiprotons, as discussed in section 3.3.

note that these parameters are model dependent and their spread may be larger at high energies. For example, δ is expected to change with energy, because an extrapolation of $\delta \sim 0.6$ to higher energies predicts large anisotropies already at 10^{15} eV, contradicting observations⁽³⁾ [52].

Eq. (3.5) sets a natural energy-dependent diffusion length scale [29, 53]

$$\lambda_D(E, E_S) = \sqrt{4K_0(t_E - t_{E_S})}, \quad (3.9)$$

where $t_E \equiv \tau_E(1 - \delta)^{-1}(E/\text{GeV})^{\delta-1}$ is the energy-dependent pseudo time. Using the models given in Table 3, we plot λ_D for detected electron with energy of 20 GeV, as a function of the injection energy in Fig. 7. A fundamental difference exists between the background and the DM contributions to the spectrum: while the injection spectrum of the former peaks at low energies (see eq. (3.14)), the one of the DM does not, as can be seen in Figs. 3,5. It then follows that while background electrons travel short distances, of order $\lambda_D \lesssim 2 - 3$ kpc, the bulk of the electrons originating from DM annihilations travel larger distances and may be created closer to the center of the Galaxy where the DM density is larger. We will return to this point shortly.

A semi-analytic solution to the diffusion equation above is found to take the form [29]

$$\Phi_{e^+}(E, r_\odot) = \frac{v_{e^+}}{4\pi b(E)} \int_E^{m_x} dE' Q_{e^+}(E', r_\odot) I(\lambda_D(E, E')). \quad (3.10)$$

where

$$I(\lambda_D) = \sum_{n,m=1}^{\infty} J_0(\zeta_n r_\odot / R) \sin(m\pi/2) \exp \left[- \left(\left(\frac{m\pi}{2L} \right)^2 + \left(\frac{\zeta_n}{R} \right)^2 \right) \frac{\lambda_D^2}{4} \right] R_{n,m} \quad (3.11)$$

and

$$R_{n,m} = \frac{2}{J_1(\zeta_n)^2 L R^2} \int_0^R r dr \int_{-L}^L dz J_0(\zeta_n r / R) \sin(m\pi(z + L)/2L) \left(\frac{\rho(r, z)}{\rho_\odot} \right)^2, \quad (3.12)$$

⁽³⁾It is possible that such a change is indicated in the ATIC-2 measurements [49] (which are not taken into account in [50]), although the large statistical uncertainties and possible normalization problems do not allow for a decisive conclusion.

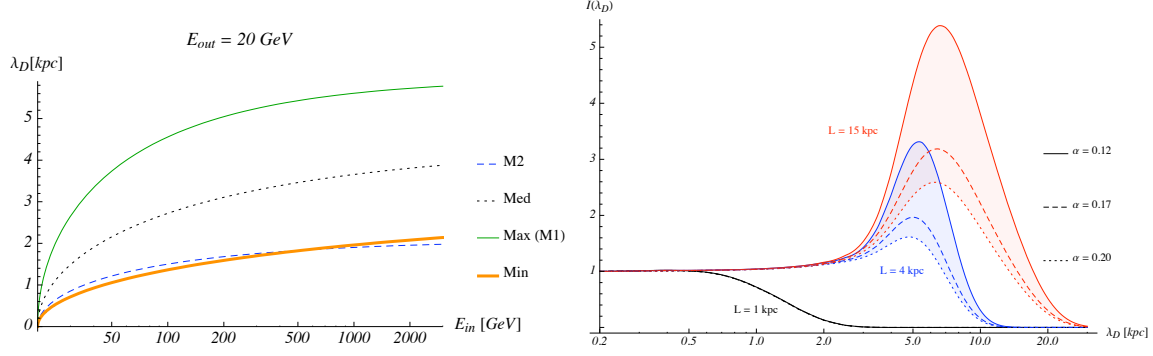


Figure 7: *Left:* The effective diffusion length, λ_D , for the propagations models we study as a function of the injection spectrum for a 20 GeV electron detected at the Earth. *Right:* $I(\lambda_D)$ for $L = 1, 4, 15$ kpc and the Einasto profile with $\alpha = (0.12, 0.17, 0.20)$.

Here J_i are the i -th order Bessel functions of the first kind and ζ_n is the n -th zero of J_0 . We plot $I(\lambda_D)$ for the Einasto profiles with $\alpha = (0.12, 0.17, 0.20)$ and in Figure 7 for the three different values of L considered here. As can be seen in the plot, $I(\lambda_D)$ may provide an enhancement to the flux if λ_D is sufficiently large. Since λ_D is largest for positrons arriving to the Earth with low energy, the spectrum tends to be softer in those cases where the positrons propagate for significant distances. This, in turn, weakens any feature that may exist at the high end of the spectrum. As suggested in Fig. 7, the effect is most significant for the MAX model. Consequently, as we shall see in Sect. 4, the MAX model fits less well to the ATIC data, but on the other hand requires a smaller cross-section to fit the PAMELA data, therefore predicting less photons from the GC. Conversely, the MIN model fits better to the ATIC data but predicts a larger cross-section and therefore a larger number of photons. This tension, in part, will be responsible for excluding significant parts of the parameter space in these DM annihilation models that try to fit PAMELA and ATIC simultaneously.

3.2.2 Experiments

The three relevant experiments for the positron study are PAMELA [1], ATIC-2 [3] and PPB-BETS [2]. The former recently provided the positron-to-electron flux ratio up to 100 GeV while the latter two experiments measure the positron plus electron flux up to energies of a few TeV.

For the purpose of testing the predictions of the theory, we need an estimation of the backgrounds. To this end, we will attempt to be as data-driven as possible. The two relevant backgrounds needed are the positron flux in the energy range between 10 to 100 GeV and the $e^+ + e^-$ flux at energies up to 1 TeV. Starting with the latter, the spectrum has been measured rather accurately. In the absence of the ATIC/PPB-BETS bump, which is apparent above ~ 100 GeV, the data fits a power-law spectrum

$$\Phi_{e^+ + e^-}(E) = A_1 \left(\frac{E}{\text{GeV}} \right)^{\gamma_1} \text{ cm}^{-2} \text{ s}^{-1} \text{ sr}^{-1} \text{ GeV}^{-1}. \quad (3.13)$$

For finding a best fit to A_1 and γ_1 we used the measurements of ATIC-2 and HEAT [54] in the energy range 20–100 GeV. The lower cutoff ensures that uncertainties from solar modulation are insignificant while the upper prevents probing the bump. We find $A_1 = 0.046 \pm 0.015$ and $\gamma_1 = -3.30 \pm 0.08$. This result is in agreement with the preliminary analysis presented by the PAMELA collaboration [55]. Taking the best fit at face value for our background is incorrect because it is impossible to disentangle the signal from background even at low energies. Therefore, when fitting together with the DM signal, we allow both A_1 and γ_1 to float around their central values given above.

No precise measurements of the positron flux exist at energies above 10 GeV. To calculate the background, we therefore use the leaky box approximation which is well suited for energies $\lesssim 100$ GeV and above $\gtrsim 10$ GeV⁽⁴⁾. We derive the prediction in Appendix A and simply quote the result here

$$\Phi_{e^+}(E) \simeq 4 \times 10^{-3} \left(\frac{E}{\text{GeV}} \right)^{-2.84-\delta \pm 0.02} \text{ cm}^{-2} \text{ s}^{-1} \text{ sr}^{-1} \text{ GeV}^{-1}. \quad (3.14)$$

which is in agreement with [28]. The parameter δ is typically of order $\delta \sim 0.6$ but for the propagation models considered above, we vary it according to the values of Table 3. As described in the Appendix, the normalization of the flux suffers from large uncertainties which arise from the assumptions in the theory and uncertainties in the measurements of the nuclear spallation cross-sections. Thus when fitting the data together with the DM signal, we allow the normalization to float around the above value. The spectral index is instead kept fixed.

3.3 Antiprotons

3.3.1 Propagation

We describe the propagation of \bar{p} at equilibrium with a diffusion equation similar to that of the positrons [56]

$$-K(E)\nabla^2 n_{\bar{p}}(E, x) + \frac{\partial}{\partial z} (V_C(z)n_{\bar{p}}(E, x)) + 2h\delta(z)\Gamma_{\text{ann}}n_{\bar{p}}(E, x) = Q_{\bar{p}}(E, x) \quad (3.15)$$

where $n_{\bar{p}}(T, \vec{r})$ is the number density of antiprotons per unit energy. As in the case of positrons, $K(E)$ is the diffusion coefficient given in Eq. (3.8). Energy loss, however, is negligible for antiprotons due to their mass and we therefore do not consider it. The last two terms on the l.h.s. of eq. (3.15) correspond to convective wind and interaction with the Interstellar Medium (ISM) in the galactic plane respectively. The convective wind is assumed to be of the form $V_C(z) = \text{sign}(z)V_C$ and is directed outwards from the galactic plane. The annihilation width between antiprotons and protons is given by

$$\Gamma_{\text{ann}} = (n_H + 4^{2/3}n_{\text{He}})\sigma_{\bar{p}p}^{\text{ann}}v_{\bar{p}}, \quad (3.16)$$

⁽⁴⁾We thank Eli Waxman and Boaz Katz for drawing our attention to this point.

where $n_{\text{H,He}} \simeq 1 \text{ cm}^{-3}$ are the hydrogen and helium number density and $v_{\bar{p}}$ is the velocity of the antiprotons. A parameterization for $\sigma_{p\bar{p}}$ can be found in [56, 57]. Both the annihilation and convective terms can be neglected at energies above $\gtrsim 10 \text{ GeV}$. Nevertheless we keep these terms for completeness.

As in the positron case, propagation takes place within the disk of half-height L and radius $R = 20 \text{ kpc}$. In order to be able to fit the data both for positrons and antiprotons and since we would like to quantify the uncertainties, we use the same models described in Table 3. An semi-analytical solution to the flux $\Phi_{\bar{p}} = v_{\bar{p}} n_{\bar{p}} / 4\pi$ is given by [58]

$$\Phi_{\bar{p}}(E, r_{\odot}) = \frac{c}{4\pi} Q_{\bar{p}} R(E) \quad (3.17)$$

where as before,

$$Q_{\bar{p}} = \frac{1}{2} \frac{\rho(r)^2}{m_{\chi}^2} \sum_k \langle \sigma v \rangle_k \frac{dN_{\bar{p}}^k}{dE}. \quad (3.18)$$

$R(E)$ encodes the astrophysical propagation information and was found to take the form [51],

$$R(E) = \sum_{n=1}^{\infty} J_0(\zeta_n r_{\odot} / R) \exp \left[-\frac{V_C L}{2K(E)} \right] \frac{y_n(L)}{A_n \sinh(S_n L / 2)} \quad (3.19)$$

with,

$$y_n(L) = \frac{4}{J_1(\zeta_n)^2 R^2} \times \int_0^R r dr \int_0^L dz J_0(\zeta_n r / R) \sinh(S_n(L - z) / 2) \exp \left[\frac{V_C(L - z)}{2K(E)} \right] \left(\frac{\rho(r, z)}{\rho_{\odot}} \right)^2, \quad (3.20)$$

$$A_n = 2h\Gamma_{\text{ann}} + V_C + K(E)S_n \coth(S_n L / 2),$$

$$S_n = \sqrt{(V_C / K(E))^2 + 4\zeta_n^2 / R^2}.$$

In Figure 8 we plot this function for the the Einasto profiles with $\alpha = (0.12, 0.17, 0.20)$ and for the propagation models of Table 3.

3.3.2 Experiments

The relevant experimental data is the recent PAMELA measurement for the antiproton-to-proton flux ratio [8] up to the energy of 100 GeV.

The proton flux, has been well measured by the BESS [59, 60] and AMS-01 [61] experiments and the best fit to the data (for demodulated protons) is of the form [62]:

$$\Phi_{p_{\text{bgd}}} = A \beta^{P_1} \mathcal{R}^{-P_2} \text{ cm}^{-2} \text{ s}^{-1} \text{ sr}^{-1} (\text{GeV/n})^{-1} \quad (3.21)$$

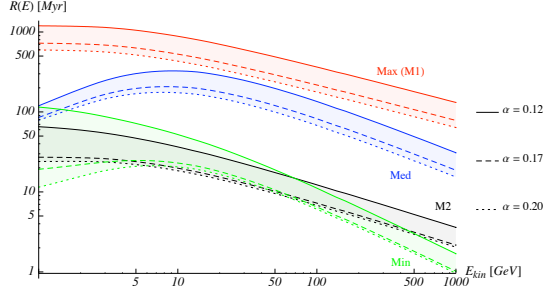


Figure 8: $R(E)$ for the propagation models we consider and the Einasto profile with $\alpha = (0.12, 0.17, 0.20)$.

where as before \mathcal{R} is the rigidity and β is the velocity. We use the following values for the coefficients

\mathcal{R}	A	P_1	P_2
$< 20 \text{ GV}$	1.94 ± 0.13	0.7 ± 0.52	2.76 ± 0.03
$> 20 \text{ GV}$	2.42 ± 0.18	0	2.84 ± 0.02

(3.22)

in agreement with [62].

The antiproton flux is known to come primarily from cosmic ray protons interacting with the ISM. Unfortunately the flux generated by this process does not have a characteristic power law shape (as many other astrophysical processes) in the range of energy that we examine. To calculate the approximate shape for the background we need to take into account the spallation cross section given in [62], and then propagate the products. Fortunately, as was found in [62], changing the model of propagation does not significantly change the shape of the antiproton flux but does change the normalization. We therefore use the results of [62], parametrized as follows [26],

$$\log_{10} \Phi_p = -1.356 + 0.114\tau - 0.645\tau^2 - 0.614\tau^3 + 0.02\tau^4 + 0.168\tau^5 - 0.038\tau^6, \quad (3.23)$$

where $\tau = \log_{10}(E/\text{GeV})$. To fit to the PAMELA data one needs to take into account solar modulation [63]. We modulate the background according to the PAMELA modulation potential $\phi = 0.58 \text{ GV}$ and allow the normalization to float.

3.4 Photons

3.4.1 Propagation

Photons from dark matter are one of the cleanest channels possible to study from the point of view of propagation. This is because once produced, photons freely travel to Earth and thus are insensitive to the propagation parameters that complicate studies of e^+ and \bar{p} . Since photons are not affected by propagation, the flux at the Earth depends only on the injection spectrum and on how many annihilations occur. While this simplifies the calculation of the photon flux, it also introduces a large amount of uncertainty. Unlike positrons and

antiprotons which reach us typically from distances less than r_\odot , photons from the galactic center, where the dark matter density is the highest, can always reach us. N-body simulations can not resolve distances less than approximately 100-200 pc (as discussed in 3.1), and thus there is a fair amount of uncertainty in the DM density profile at the galactic center.

The differential photon flux (in units of $\text{cm}^{-2} \text{s}^{-1} \text{sr}^{-1} \text{GeV}^{-1}$) is given by,

$$\Phi_\gamma = \frac{r_\odot}{4\pi} Q_\gamma \bar{J} \Delta\Omega, \quad (3.24)$$

As before, Q_γ is the photon source encoding the particle physics contribution to the flux,

$$Q_\gamma = \frac{1}{2} \frac{\rho(r)^2}{m_\chi^2} \sum_k \langle \sigma v \rangle_k \frac{dN_\gamma^k}{dE}. \quad (3.25)$$

Much like $I(E)$ and $R(E)$ in the positron and anti-proton case, \bar{J} encapsulates the astrophysics dependence and is given by,

$$\bar{J} = \frac{1}{\Delta\Omega} \int d\Omega \int_{\text{line-of-sight}} \frac{dl}{r_\odot} \left(\frac{\rho(r)}{\rho_\odot} \right)^2. \quad (3.26)$$

where $\Delta\Omega$ is the opening solid angle for a given experiment. The flux received in a given direction is proportional to the integral over the line-of-sight of the DM density squared. By writing the photon flux in this factorized form we simply need to compute the \bar{J} for a given experiment and profile.

In principle, for cuspy profiles the integral in Eq. 3.26 could diverge. For the profiles that we consider \bar{J} in fact does not diverge. However, as discussed in 3.1, depending on the assumed regulation of the DM density inside of $\mathcal{O}(100)$ pc, the actual value of \bar{J} computed can vary significantly as a function of r_c in Eq. 3.4. We will quantify this uncertainty further in Section 4.2 when we show the dependence of photon flux on the choice of the dark matter density profile.

3.4.2 Experiments

The experiments that we will be primarily concerned with are those that measure high energy gamma rays. Specifically we will focus on the HESS experiment which is the most sensitive to high mass DM annihilation. The FERMI-LAT experiment will also be of importance in the near future and we discuss it further in Section 5. If one is looking for signals of DM annihilation into photons, the best place to look is in regions of potential high DM density with small astrophysical backgrounds. For instance high mass/light ratio dwarf spheroidal galaxies [64] or subhalos of our galaxy [65] are both prime candidates for a clean signal of DM annihilations. However, for the purpose of constraining models of DM, it is more important to observe regions that have effectively a large \bar{J} for sufficiently long time. For the HESS experiment this is found in two regions, the Galactic Center (GC) [66] and the Galactic Ridge (GR) [67].

The GC as studied by HESS has a $\Delta\Omega = 10^{-5}$. To calculate \bar{J} for the Galactic Center one can write

$$\int d\Omega = \int_{\cos\psi}^1 2\pi d(\cos\psi') , \quad (3.27)$$

$$\Delta\Omega = 2\pi(1 - \cos\psi) , \quad r = \sqrt{r_\odot^2 + l^2 - 2lr_\odot \cos\psi'} . \quad (3.28)$$

The GC was observed by HESS for 48.7 hours during 2004, and is cataloged as J1745-290.

The GR is a larger region that includes the GC. It is defined in galactic latitude and longitude as the region $|l| < 0.8^\circ$ and $|b| < 0.3^\circ$. The GR has several known suspected point sources including J1745-290 that the HESS experiment modeled in order to subtract it in [67]. The experiment fits a point source to two specific regions, J1745-290 and another source, G0.9+1, that lie within the Ridge. The best fit for these sources was then subtracted and the differential flux dN/dE was given for the remaining portion which defines the Ridge. Unfortunately the dN/dE for each galactic latitude and longitude has not been published and therefore one can not mimic their subtraction scheme. However, since the hypothesized point sources are the dominant sources of photons we can excise these entirely without introducing a large amount of uncertainty into the calculation of \bar{J} . Additionally, beyond these partial subtractions, a further subtraction to reduce systematics is also performed. The HESS experiment observes the regions $0.8^\circ < |b| < 1.5^\circ$ and uniformly subtracts this “background” from the GR data. We will perform this same subtraction when plotting the observed photon flux. To calculate the value of \bar{J} for the GR (which is a rectangle not a circle) we use a slightly different form of $d\Omega$. For a region defined by longitudinal and latitudinal boundaries $|\theta| < \Delta l$, $|\psi| < \Delta b$, we have,

$$\int d\Omega = 4 \int_0^{\Delta l} d\theta' \int_0^{\sin\Delta b} d(\sin\psi') , \quad (3.29)$$

$$\Delta\Omega = 4\Delta l\Delta b , \quad r = \sqrt{r_\odot^2 + l^2 - 2lr_\odot \cos\psi' \cos\theta'} . \quad (3.30)$$

To finish our discussion of the experimental inputs for photons we will tabulate the \bar{J} calculated for the various experiments and profiles in Table 4.

3.5 Neutrinos

3.5.1 Propagation

Dark Matter annihilations can also produce neutrinos. After being produced, neutrinos propagate till the Earth where they are detected. The standard strategy to detect these neutrinos is to look at those that convert in rock nearby the detectors and observe the charged leptons, in particular muons. Therefore the quantity actually measured is the muon flux, that can be related to the neutrino flux at production by

$$\frac{d\Phi_\mu}{dE_\mu} = R(E_\mu) \int_{E_\mu}^{m_\chi} dE_\nu \sum_{i=e,\mu,\tau} \frac{d\Phi_{\nu_i}}{dE_\nu} P_{i\rightarrow\mu} \sum_{N=p,n} \rho_N \frac{d\sigma_{\nu N}(E_\mu/E_\nu)}{dE_\mu} + (\nu \leftrightarrow \bar{\nu}) \quad (3.31)$$

Location	Profile	\bar{J}
Galactic Center ($\Delta\Omega = 2 \cdot 10^{-5}$)	Cored isothermal	13.6
	NFW	4076 – 10170
	Moore	13128 – 51388
	Einasto $\alpha = 0.17$	6610
	Einasto $\alpha = 0.12$	65500
	Einasto $\alpha = 0.2$	2306
Galactic Ridge	Cored isothermal	0.02
	NFW	1295 – 1541
	Moore	3836 – 5653
	Einasto $\alpha = 0.17$	1614
	Einasto $\alpha = 0.12$	10886
	Einasto $\alpha = 0.2$	602

Table 4: The values for \bar{J} for the various galactic regions we consider. For the NFW and Moore profiles in the Milky way, we show the range for J for $0 \leq r_c \leq 0.1$ kpc.

where $d\Phi_{\nu_i}/dE$ is the flavor specific neutrino flux, the sum is taken over all the leptonic flavors and the term $P_{i \rightarrow \mu}$ comes from the fact that neutrinos oscillate during their travel⁽⁵⁾. The muon production cross section in neutrino nucleon interactions is denoted by $\sigma_{\nu N}$ [68,69], while $\rho_{p,n}$ are the proton and neutron number densities (taken to be equal for standard rock). Finally $R(E)$ is the muon range [42], i.e. the distance traveled by a muon of energy E before stopping or before getting below the detection energy threshold of the experiment.

3.5.2 Experimental Status

Good places to look for neutrinos produced in DM annihilations are the GC (like in the case of photons) but also the Sun and the Earth, where DM may be trapped in the gravitational field and their density may grow large enough to allow for a sizable annihilation rate. Another signal that one can look for is the total diffuse neutrino flux [70].

The flux coming from the Sun and the Earth has been recently re-investigated in light of the PAMELA and ATIC [71]. In particular the authors of [72] have found that for DM annihilating mainly into leptonic final states, the neutrino flux from the Sun and the Earth is out of reach of IceCube unless the DM annihilates directly into a pair of neutrinos. In our case IceCube can still be of relevance if the ϕ mass is high enough in the multi-GeV range where hadronic decays are also allowed, but in this case the bounds on the photon flux will be also very strong as it will be shown in Sect. 4. For this reason here we will only discuss the neutrino flux coming from DM annihilations in the Galactic Center.

⁽⁵⁾ $P_{i \rightarrow \mu}$ is determined only by the mixing angles since the baseline is very long. For simplicity we have taken $\theta_{13} = 0$.

In this case the present bounds comes mostly from detectors located in the northern hemisphere, since there the Galactic Center is below the horizon most of the time. In particular the current best limit is from SuperKamiokande [73], which looks at the up-going muons produced in the rocks below the detector. The collaboration reports an upper bound on the total muon flux above a threshold of 1.6 GeV, as a function of the half-opening angle of a cone pointing towards the center of the Galaxy. As we show in the next Section, this bound is not powerful enough to give any appreciable constraints on the parameters of our module.

In the future this limit will be improved by Antares, a neutrino telescope in deep Mediterranean waters, which started taking data in 2007, and on a longer timescale by Km3Net and Megaton-size neutrino detectors like Hyper-Kamiokande.

4 Results

In this section we combine the particle physics inputs that were calculated in Section 2 and the propagation methods that were discussed in Section 3 to calculate the fluxes for various experiments. We are primarily interested in answering the following questions:

1. Given our particle physics framework, what is the preferred parameter space that can explain PAMELA and ATIC/PPB-BETS?
2. Given this parameter space, what are the regions that are compatible with existing searches for γ 's and ν 's?

To answer these questions we need to define what we mean by the preferred parameter space and how we bound it. We implement a χ^2 function in order to fit a given data set with our particle physics and background parameters (the relevant set is shown in Table 5). To understand the allowed regions and how the parameters affect the fluxes we perform the following procedure. We pick a parameter of interest and we marginalize over all the other parameters. We then extract the fluxes as a function of the chosen parameter. In this section we will only marginalize a χ^2 function for the PAMELA and ATIC/PPB-BETS data. We then plot the resulting fluxes as a function of this parameter both for PAMELA, ATIC and PPB-BETS, and for HESS and SuperK data, where applicable. The allowed parameter regions are those points with good fits that do not conflict with the HESS and SuperK data.

Below, we separate the parameters that we are interested in into two categories: particle physics discussed in Section 4.1, and astrophysics discussed in Section 4.2. By examining these parameters independently, we study their influence on the fluxes, and the uncertainties in our predictions. We postpone the fits to all data and their implications to Section 5.

4.1 Particle Physics

4.1.1 Light Gauge Boson Mass

In this section we isolate the effects of varying the light gauge boson mass, m_ϕ , on the fluxes. To understand how the particle physics parameter m_ϕ influences the results, we fix both the

Background Parameters	$N_{e^+}, N_{e^++e^-}, N_{\bar{p}}, \gamma_{e^++e^-}, N_{\gamma}, \gamma_{\gamma}$
Particle Physics Parameters	$m_{\chi}, m_{\phi}, \langle\sigma v\rangle, R_{\text{SM}}, \alpha_{\text{DM}}$

Table 5: A summary of the parameters used for fitting the data.

m_{ϕ} (GeV)	m_{χ} (TeV)	$10^{23} \times \langle\sigma v\rangle(\text{cm}^3\text{s}^{-1})$	$(N, \gamma)_{e^++e^-}$	N_{e^+}	χ^2/dof
0.2	0.96	0.94	(0.6,-3.21)	0.7	1.9
0.5	1.54	2.70	(0.6,-3.20)	0.6	2.1
1.2	1.46	2.51	(0.6,-3.19)	0.6	2.1
8	2.3	5.41	(0.3,-3.06)	0.2	2.7
15	3.5	9.17	(0.3,-3.06)	0.3	2.9

Table 6: The best fit values for the plots in Fig. 9. $\gamma_{e^++e^-}$ is the best fit value for the spectral index of the background electron plus positron flux. N_i is the fraction of the normalization found for the best fit background without a DM signal. These normalizations are found in Section 3. Finally, the SM ratios, R_{SM} are all smaller than 1%. and so are not shown.

dark matter profile and propagation model and marginalize over the rest of the parameters. We choose the Einasto profile with $\alpha = 0.17$ and the MED propagation model.

In Fig. 9 we plot the best fits for PAMELA, ATIC/PPB-BETS as well as the bounds from neutrinos and HESS experimental data for the GC and GR in Figure 9. In Table 6 we give the best fit values for these plots together with the χ^2/dof . The number of dof's that go into our fit is 33, from assuming 40 independent measurement points (coming from PAMELA, ATIC and PPB-BETS) and 7 variables. As one can see, the χ^2/dof is typically of order 2 which for 33 dof's is a rather poor fit. We trace this fact to the two features in the ATIC data: The plateau above 100 GeV and a bump at around 500 GeV which cannot be explained together with only one DM state. It remains to be seen if these two features in the spectrum survive future measurements. In the mean time, we view the values of χ^2 as no more than an indicator for comparing different models.

The values plotted for m_{ϕ} are discussed in Section 2. From Table 6 we see that small m_{ϕ} fit the data better. This is because as m_{ϕ} increases the positron spectrum becomes softer due to new kinematically accessible decay channels. As m_{ϕ} increases dN/dx increasingly deviates from the relatively flat spectrum when ϕ only annihilates into $e^+ + e^-$. Compared to the flat dN/dx , to fit PAMELA and ATIC/PPB-BETS for higher m_{ϕ} , one needs a combination of boost factor and increase in mass to attempt to make up for the softer spectrum.

For the case of 8 and 15 GeV, the large DM mass (and therefore the poor fits) is driven by the more constraining antiproton flux. Indeed, for m_{ϕ} above twice the proton mass, the PAMELA antiproton-to-proton spectrum becomes an even stronger constraint. In particular, for $m_{\phi} = 8$ and 15 GeV, the DM mass must be sufficiently large in order to avoid generating

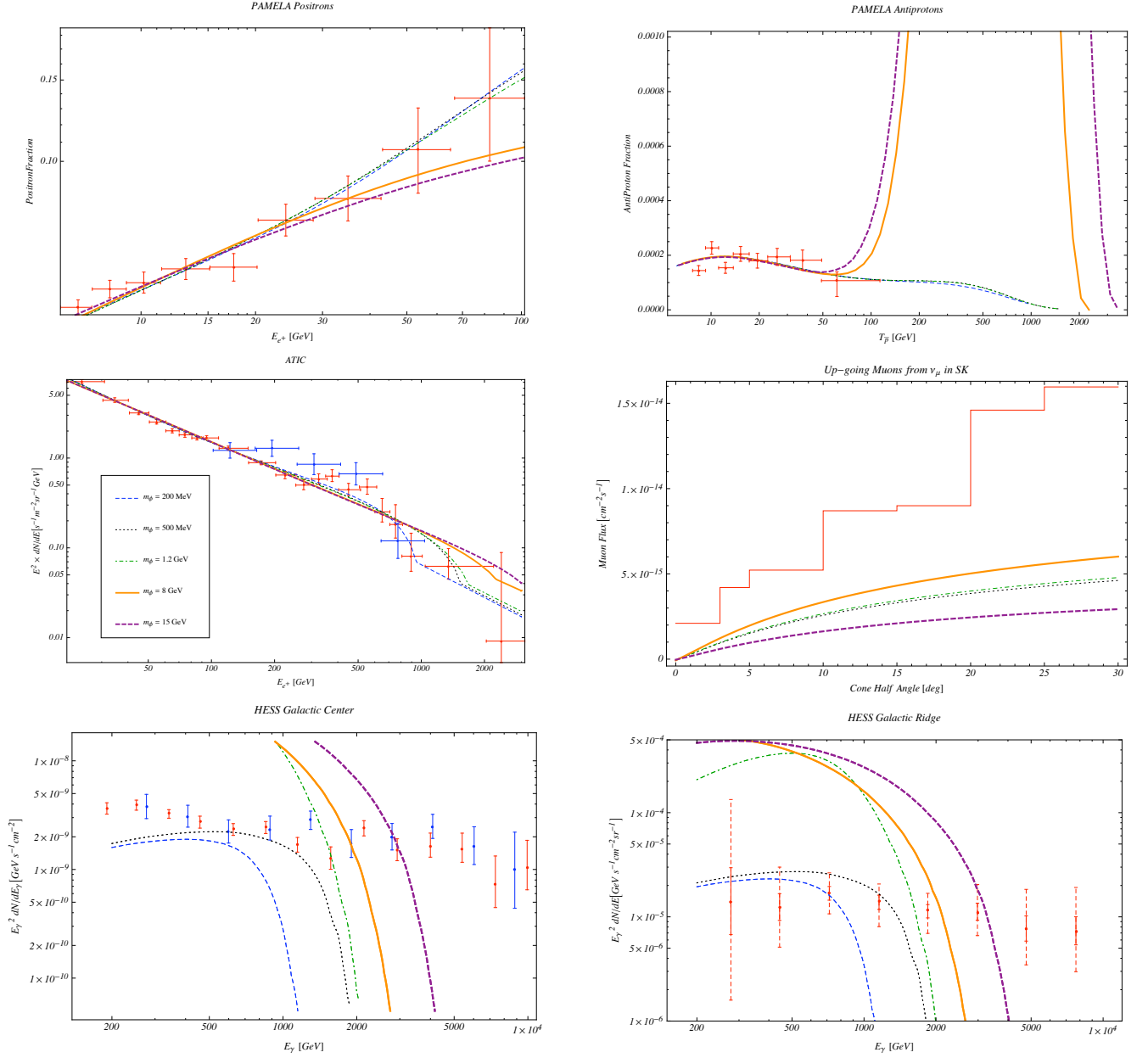


Figure 9: Best fit to the PAMELA, ATIC and PPB-BETS experiments for Einasto profile with $\alpha = 0.17$, propagation model MED fixed and $m_\phi = 0.2, 0.5, 1.2, 8, 15$ GeV. The predictions for neutrinos and photons are shown in the last three plots overlayed with the SuperK and HESS measurements respectively. Around each bin of the HESS data, we indicate the 1σ (solid) error bar. For the GR we also indicate the 3σ (dashed) error bar. The best fit parameters are shown in Table 6.

too many antiprotons at energies within the PAMELA reach. This is indeed apparent in Fig. 9 which shows a large bump in the antiproton spectrum just above the PAMELA 60 GeV bin. Whenever the antiproton constraint pushes the mass too high, denying a good fit to the positron data, the overall fit for these masses is significantly worse.

It is interesting to note that a $2 - 3$ TeV DM particles is sufficient in order to avoid the antiproton bound in the case of 8 GeV light gauge field. This is in contrast to a 10 TeV DM required in the case of direct W and Z decays as in the SM [74]. A simple way to understand this, is to notice that the anti-proton spectrum is (almost) identical in both cases when viewed in the gauge boson restframe. The spectrum must then be boosted to the lab frame, which introduces a boost factor of order m_χ/m_ϕ . In both the SM and with light gauge fields, this factor is of order 10^2 which is the minimum required in order to avoid the PAMELA antiproton bound, effectively increasing the QCD scale above 100 GeV. Thus we conclude that with light gauge fields the bound is easy to overcome with, $m_\chi/\text{TeV} \simeq m_\phi/(10 \text{ GeV})$.

The photon predictions for the HESS measurements from the GC and GR are shown in the last two plots. It is apparent that the GR is more constraining than the GC. Moreover, we do not include photons from ICS which may strengthen the bound. Heavy vector bosons, at or above 1.2 GeV are excluded by HESS. On the other hand, the 200 and 500 MeV vector bosons are marginally within 3σ error bars of the measured data. Clearly, once a background is added to the fit the data, the tension becomes larger, as the background is required to be sufficiently large to allow for a good fit to the data points above m_χ where a DM signal is absent. We therefore conclude that some further suppression (e.g. local boost factor or shallower DM profile) is required to render these models viable. We return to this issue and quantify the suppression in Section 5.

Finally we note that the Neutrino bound is sufficiently weak to evade and therefore adds no further constrain on the model.

4.1.2 Hidden Sector Shower

Let us now study the effects of showering in the dark sector. As in the case where we isolated the effects of m_ϕ , we fix an Einasto profile with $\alpha = 0.17$ and MED propagation, then marginalize over the other parameters and plot the fluxes for different values of α_{DM} . Specifically to illustrate the effects of the shower we find the best fit for $\alpha_{DM} = 10^{-3}$ and then keeping the same parameters but varying the gauge coupling we plot the resulting fluxes in Fig 10. To illustrate the effect of showering on the antiprotons, we repeat the same procedure with $m_\phi = 8 \text{ GeV}$, showing only the antiproton flux ratio.

There are several effects worth noting. The first, is that showering in the DM sector implies a softer electron, positron and antiproton spectra. As discussed in the previous section, a softer spectrum fits ATIC less well. Moreover, if antiprotons are produced the softening of their spectrum forces m_χ to be higher. On the other hand, softening of the spectrum implies more electrons and positrons at the PAMELA energies, which explains the increase in flux for larger α_{DM} as can be seen in the first plot of Fig. 10.

On the other hand, as we will see in Section 5, models where showering in the DM sector is significant, tend to fit the data better when taking the HESS measurements into account.

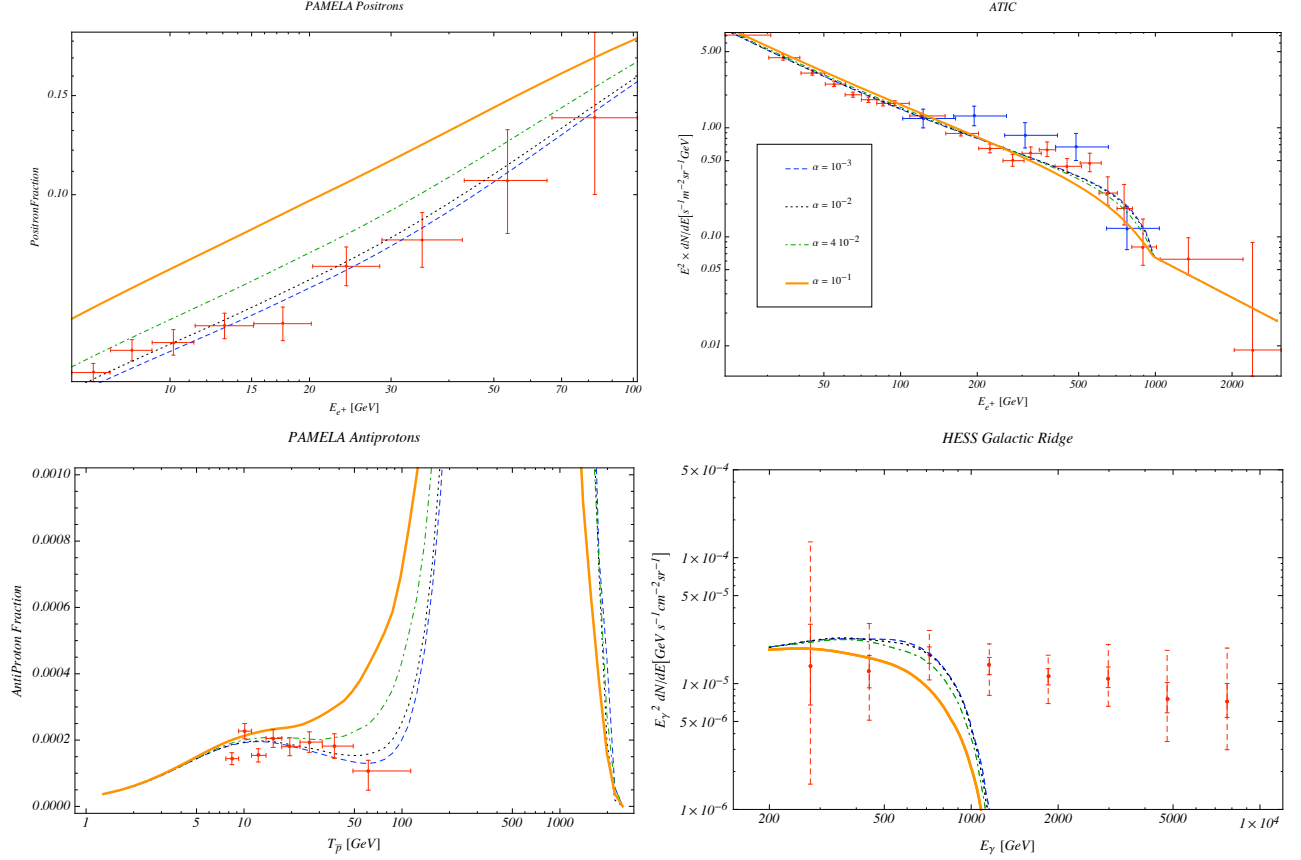


Figure 10: Effects of dark sector showering. Plotted are the PAMELA, ATIC/PPB-BETS and HESS GR data for models with Einasto profile with $\alpha = 0.17$, MED propagation model, $m_\phi = 200$ MeV, $m_\chi = 1000$ GeV. and $\alpha_{\text{DM}} = 0.001, 0.01, 0.04, 0.1$. These parameters are the best fit for the $\alpha_{\text{DM}} = 0.001$ case. In this model antiprotons are not produced. Instead we show the effect on antiprotons for the case of $m_\phi = 8$ GeV. Around each bin of the HESS data, we indicate the 1σ (solid) and 3σ (dashed) error bar.

The reason for this is that the photon spectrum is softened as well due to the showering. This is apparent in the last plot of Figure 10 where we see that larger α_{DM} implies less photons. Since the strongest constraints come from photons, it is preferred (for minimizing the χ^2) to allow for softening of both the photons and electrons, so that the ATIC fit is poorer but the photon fit is better.

4.1.3 SM Ratio and Direct Decays

We now study the implications of DM directly annihilating into SM particles. A similar study was presented in [15, 74]. Here we confirm part of their results, while emphasizing the difference between the predictions of direct annihilations versus those through light vector

fields.

To this end, we concentrate on two possibilities, namely direct couplings to SM gauge bosons, and direct couplings to e^\pm . From the point of view of the PAMELA results, the latter is preferable as it does not incorporate any hadronic decays and therefore no anomalous antiproton flux. On the other hand the former is guaranteed to exist at some level if the ϕ can mix with the SM vector bosons.

To emphasize the difference between $2 \rightarrow 2$ and $2 \rightarrow 4$ decays, we compare the predictions of direct annihilations to the case of $m_\phi = 200$ MeV, for which only e^\pm production is kinematically accessible. As was discussed in subsection 4.1.1, this is also the model which best fits the data if shower is not included. The best fit parameters are shown in the first line of Table 6. The χ^2 value for the best fit of the direct decay is found to be $\chi/\text{dof} = 2.6$ which is worse than that of the $2 \rightarrow 4$ case. The best fit parameters are,

$$m_\chi = 680 \text{ GeV}, \quad \langle \sigma v \rangle = 6.34 \times 10^{-23} \text{ cm}^2, \quad R_{\text{SM}} = 2\%, \quad (4.1)$$

$$(N, \gamma)_{e^+e^-} = (0.9, -3.27), \quad N_{e^+} = 1. \quad (4.2)$$

As in previous cases, N_i denotes the fraction of the normalization found for the backgrounds, while $\gamma_{e^+e^-}$ is the spectral index for the correspond background flux.

In Fig 11 we plot the two models together with the PAMELA positrons, ATIC/PPB-BETS and HESS measurements. While the fit to the ATIC/PPB-BETS data is better, it is clear that direct coupling to e^\pm does not fit the PAMELA data well. The reason for this can be traced back to the injection spectrum for the e^\pm line shown in Fig. 4: Since the decay is $2 \rightarrow 2$, the ATIC data dictates a low DM mass around the bump. For such a low mass, the hard form of the spectrum is then insufficient to explain the PAMELA anomaly.

To partly compensate for the injection spectrum, a large cross-section, is required. This, together with the very hard spectrum explains the large number of photons predicted in such a case, as shown in Fig. 11. Clearly, this model is in contradiction with the HESS data and is therefore excluded [15].

Next we would like to understand the extent to which the DM particle can couple to the SM gauge vector bosons. A known constraint is that the massive SM gauge fields decay into hadronic states and may therefore produce an unacceptable excess of antiprotons. It is interesting to quantify this statement. We do that in Figure 12 where we plot 2D confidence level contours for the allowed regions of parameter space with $m_\phi = 200$ MeV and Einasto $\alpha = 0.2$ profile, as a function of m_χ and R_{SM} . We see that while the best fit value prefers 5% of SM annihilations, at 1σ one can have as much as 25%. While in this plot we did not attempt to fit the HESS data, we have checked that models which fit the HESS data without difficulty, such as Einasto profile with $\alpha = 0.2$, do not change this result significantly (see Sect. 5). Conversely, models that are only marginally consistent with HESS, such as the Einasto profile with $\alpha = 0.17$, reduces the parameter space almost entirely. For model building this result implies that the DM particle must couple only weakly to the SM. This can be implemented either by coupling χ to SM singlets, or otherwise making α_{DM} sufficiently large.

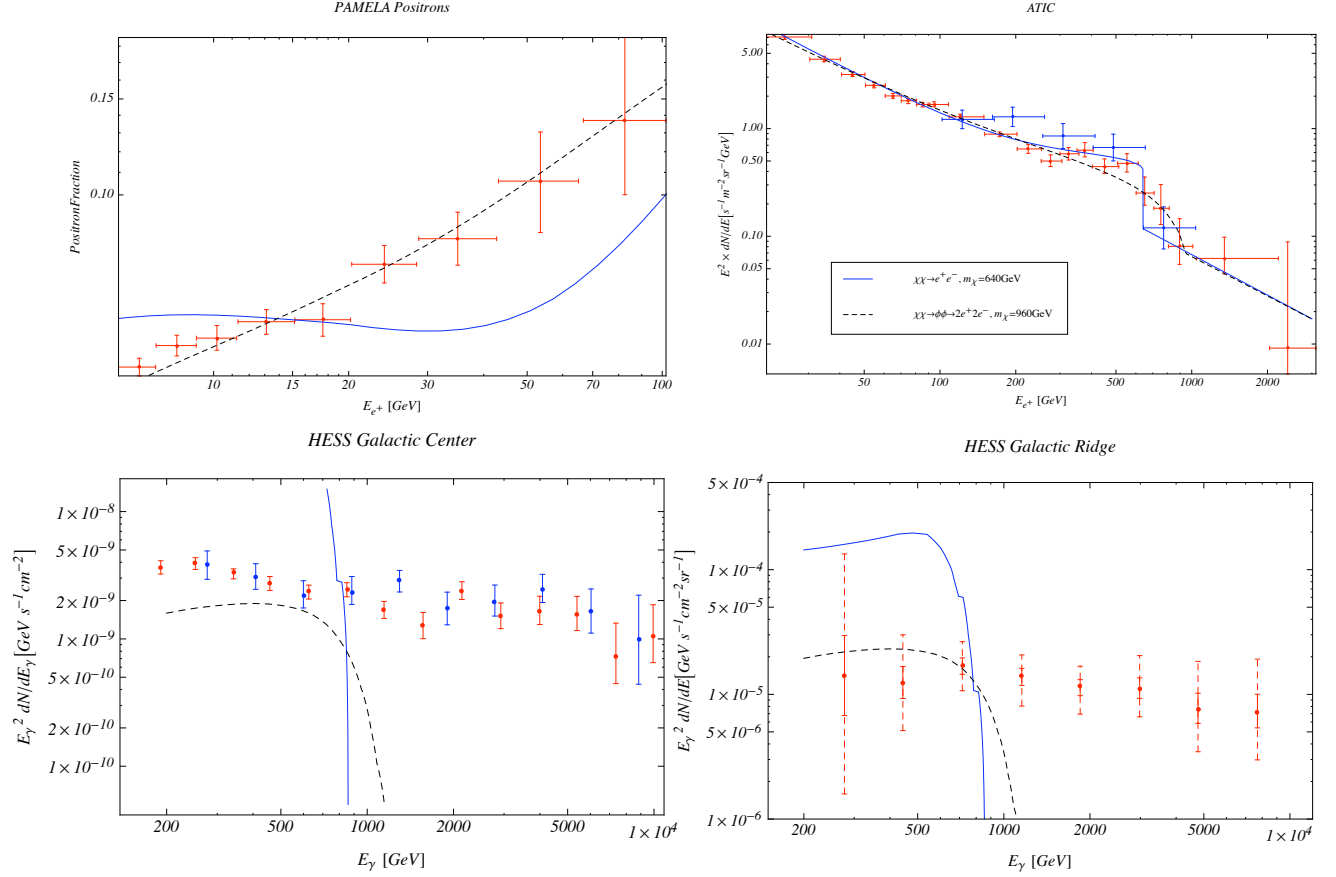


Figure 11: A comparison between an e^+e^- annihilation channel and the best fit result for annihilation through two 200 MeV light state which each decays into e^+e^- . The details of the $2 \rightarrow 4$ model is shown in Table 6. The fit done with the Einasto profile with $\alpha = 0.17$ and propagation model MED fixed. The antiproton and neutrino spectrum is not shown since those are not produced due to kinematics. The predictions for photons are shown in the last two plots overlayed with the HESS measurements. Around each bin of the HESS data, we indicate the 1σ (solid) and 3σ (dashed) error bar. The best fit parameters are shown in Table 6.

4.2 Astrophysics Uncertainties

4.2.1 Profile

We now study the dependence of the predictions on the DM profile. As discussed in Section 3.1, current N-body simulations do not allow us to pin-point the precise DM profile. The main difficulty for these simulations is the resolution, which does not allow one to probe the DM distribution within ~ 100 pc from the GC. Moreover, baryons are not incorporated in simulations, while they may play important roles in the GC.

The effective diffusion scale for electrons is smaller than the distance of the solar system

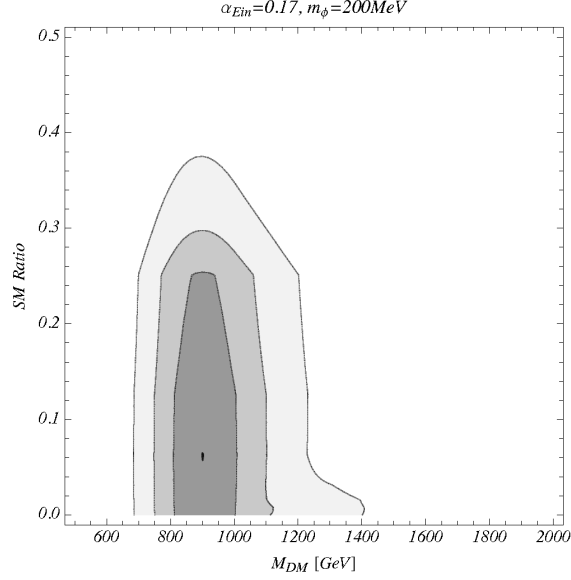


Figure 12: A confidence level contour plot for $m_\phi = 200$, and Einasto $\alpha = 0.2$ as a function of m_χ and R_{SM} . The contours correspond to the 68%, 95% and 99% confidence levels.

from the GC and therefore their flux is not sensitive to the large uncertainties in the inner DM profile. On the other hand, photons do not diffuse and therefore most of them come from the center where the bulk of the DM lies. This then allows one to probe and constrain theories of DM in conjunction with the DM profiles that are extracted from N-body simulations.

To study the profile dependence we take $m_\phi = 500$ MeV, and scan over the six profiles: NFW [30], Moore [32], Isothermal Core [34] and Einasto [36] with $\alpha = (0.12, 0.17, 0.20)$, fitting the rest of the parameters to PAMELA and ATIC/PPB-BETS. Because we do not attempt to fit to the HESS data here, the fits are almost identical in their resulting parameters. We find (on average),

$$m_\chi = 1540 \text{ GeV}, \quad \langle \sigma v \rangle = 2.88 \times 10^{-23} \text{ cm}^2, \quad R_{\text{SM}} = 0, \quad (4.3)$$

$$(N, \gamma)_{e^+e^-} = (0.6, -3.21), \quad N_{e^+} = 0.4 - 1. \quad (4.4)$$

In Figure 13, we show the usual plots together with the predictions for the photons. The bands in these plots show the sensitivity of the NFW and Moore profiles to the distance $0 \leq r_s \leq 100$ pc from the center of the Galaxy, below which we regularize the profiles as discussed in Section 3.1. No such regularization is performed for the Einasto and Isothermal profiles since they do not diverge at the GC.

The HESS plots in the figure demonstrate the strength of the constraint arising from the HESS data, the strongest coming from the GR. These essentially constrain \bar{J} defined in Eq. (3.26). We stress that, as before, the expected photon spectrum shown does not include any background. Adding such a background is crucial in order to fit the measured data at energies above that of the DM. In such a case, the constraints are much stronger. We return to this issue in the next section.

Even without background we learn that both the Moore and Einasto with $\alpha = 0.12$ are excluded by more than 3σ while NFW and Einasto with $\alpha = 0.17$ are above the data, but within the 3σ error bars. As we shall see below, once background is added, these profiles are excluded unless some kind of suppression is in place, like the hidden sector shower, a local boost factor, etc..

It is important to note that independently of \bar{J} , these photon predictions provide an conservative estimation of the signal for two reasons: (i). We have not taken ICS into account. Such radiation is certainly important at low energy, but could also be important at intermediate scales. (ii). As discussed in Section 3.4, for the GR, we do not include any photons coming from the GC. On the other hand, the GR measurements count photons from the center, after removing a dominant background source [67]. This is approximately a 10% effect.

The annihilating DM scenario studied here is somewhat complimentary to the studies of [15]. We therefore conclude that the HESS measurements together with PAMELA and ATIC/PPB-BETS, strongly constrain the possible DM profiles in the case of annihilating DM scenarios. While not excluded, future experiments may strengthen the bounds considerably.

4.2.2 Propagation

Finally, let us consider the uncertainties arising from the propagation parameters. Here we stress again that our choice of propagation model already entails some uncertainties as our understanding of Cosmic ray propagation is not complete. Nevertheless, we show how our predictions vary as we change the parameters as discussed in Section 3.2.1, which were shown to span the possible positron and antiproton spectra. Such uncertainties have been studied extensively [28, 29, 75–77] so we only concentrate on our predictions.

As in previous sections, we take our benchmark point, $m_\phi = 200$ MeV and the Einasto $\alpha = 0.17$ profile, and fit the rest of the parameters for the four propagation models, MIN/MED/MAX(M1)/M2. The best fit values of the parameters are shown in Table 7 and the predictions are shown in Figure 14. Even though antiprotons are not produced from DM annihilations through the light gauge fields, some of the best fit models require a non-negligible SM couplings and consequently antiprotons are produced as can be seen in the plots.

The tension anticipated in Section 3.2.1 is now apparent: because of the enhancement of the flux through $I(\lambda_D)$ for large λ_D in the MED and MAX cases, the electron spectrum in that case is softer (recall that the diffusion length, λ_D , is larger for lower detected energies). Therefore, for these propagation models the feature in the high energy spectrum is less pronounced and so the fit for ATIC/PPB-BETS is not as good. On the other hand, due to the soft spectrum, a smaller cross-section is needed to fit PAMELA and therefore less photons are predicted for these models. This is consistent with Figure 14. Moreover, in the MED/MAX models the spectral index for the background $e^+ + e^-$ flux is harder to compensate for the bad fit to the ATIC bump.

We find it is easier to evade the HESS constraints if propagation of positrons is closer to the MAX model described above, and in particular if the dependence of the escape time of

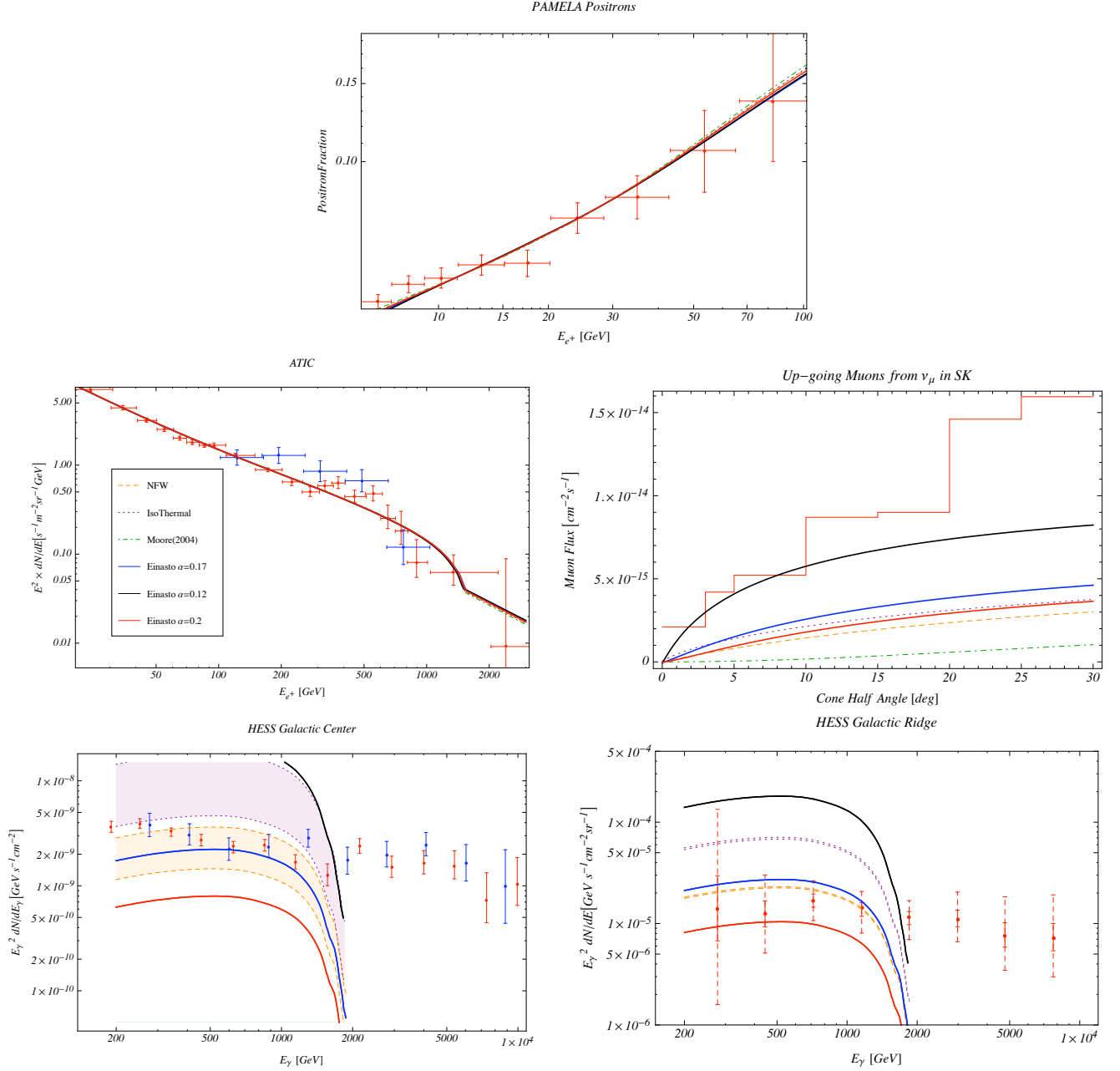


Figure 13: Best fit to the PAMELA, ATIC and PPB-BETS experiments for different DM profiles and with $m_\phi = 500$ MeV and $m_\chi = 1.54$ TeV. Propagation model is taken to be MED. No antiproton bound exists due to kinematics. The bands in the photon predictions come from regulating the NFW and Moore profiles with $0 \leq r_s \leq 100$ pc. Around each bin of the HESS data, we indicate the 1σ (solid) and 3σ (dashed) error bar. The best fit parameters are shown in Eqs. (4.3), (4.4).

Model	m_χ (TeV)	$10^{23} \times \langle\sigma v\rangle (\text{cm}^3\text{s}^{-1})$	$(N, \gamma)_{e^++e^-}$	N_{e^+}	R_{SM}	χ^2/dof
MIN	0.90	1.15	(0.9,-3.28)	1.9	6%	1.8
MED	0.96	0.94	(0.6,-3.21)	0.7	1%	1.9
MAX(M1)	1.38	0.38	(0.4,-3.10)	1.4	1%	2.3
M2	2.3	1.44	(1,-3.33)	0.9	11%	2.0

Table 7: The best fit values different propagation models with $m_\phi = 200$ MeV, shown in the plots of Fig. 14. $\gamma_{e^++e^-}$ is the best fit value for the spectral index of the background electron plus positron flux. N_i is the fraction of the normalization found for the best fit background without a DM signal. These normalizations are found in Section 3.

Cosmic rays on the energy is weaker (smaller δ). Interestingly, it is likely that the behavior of the escaping time flattens somewhere below the knee at 10^{15} eV [52]. Moreover, uncertainties in the spallation cross-sections may point towards a smaller δ .

5 Implications and Future Directions

In this section we discuss the implications for models that attempt to explain the PAMELA and ATIC/PPB-BETS excesses, based on the results shown in Section 4. In Section 4 we have shown by varying the particle physics and astrophysics parameters that only certain regions of parameter space can satisfy all the various experimental constraints. Specifically, the most difficult constraints arose from the HESS’s measurement of the GC and GR regions. Indeed it was initially believed that hadronic activity from DM was needed to be suppressed in order to avoid creating an excess in the antiproton flux. Conversely, m_χ could be pushed to scales of order 10 TeV, to avoid the bound. As we have demonstrated in Section 4, one *can* tolerate antiprotons without having to raise m_χ significantly above the mass scale of the purported ATIC/PPB-BETS excesses. On the other hand, the real hadronic danger comes from π^0 decays which produce a significant amount of photons. By scanning over m_ϕ we have shown that one does in fact need a model that goes ultimately almost exclusively into purely leptonic final states.

In several recent papers [15, 16] it was also argued, or indirectly demonstrated, that the high energy photons rule out models that try to explain both the PAMELA and ATIC/PPB-BETS excesses. This is not a conclusion that we agree with. These papers primarily investigated the case where DM annihilated directly into leptons. As shown in Section 2.1, the dN/dx calculated in these cases is actually quite different, and a simple rescaling of the overall rate does not interpolate between the case of directly annihilating into leptons and annihilating through ϕ . To demonstrate that there exist viable models that satisfy the high energy constraints we show a best fit point from the scan over our parameters. In Figure 15 this point is shown where $m_\chi = 1$ TeV, $m_\phi = 200$ MeV, $\langle\sigma v\rangle = 8.2 \cdot 10^{-24} \text{ cm}^3/\text{s}$ and $\alpha_{DM} = 0.04$, for an Einasto profile with $\alpha = 0.2$ and the MED propagation parame-

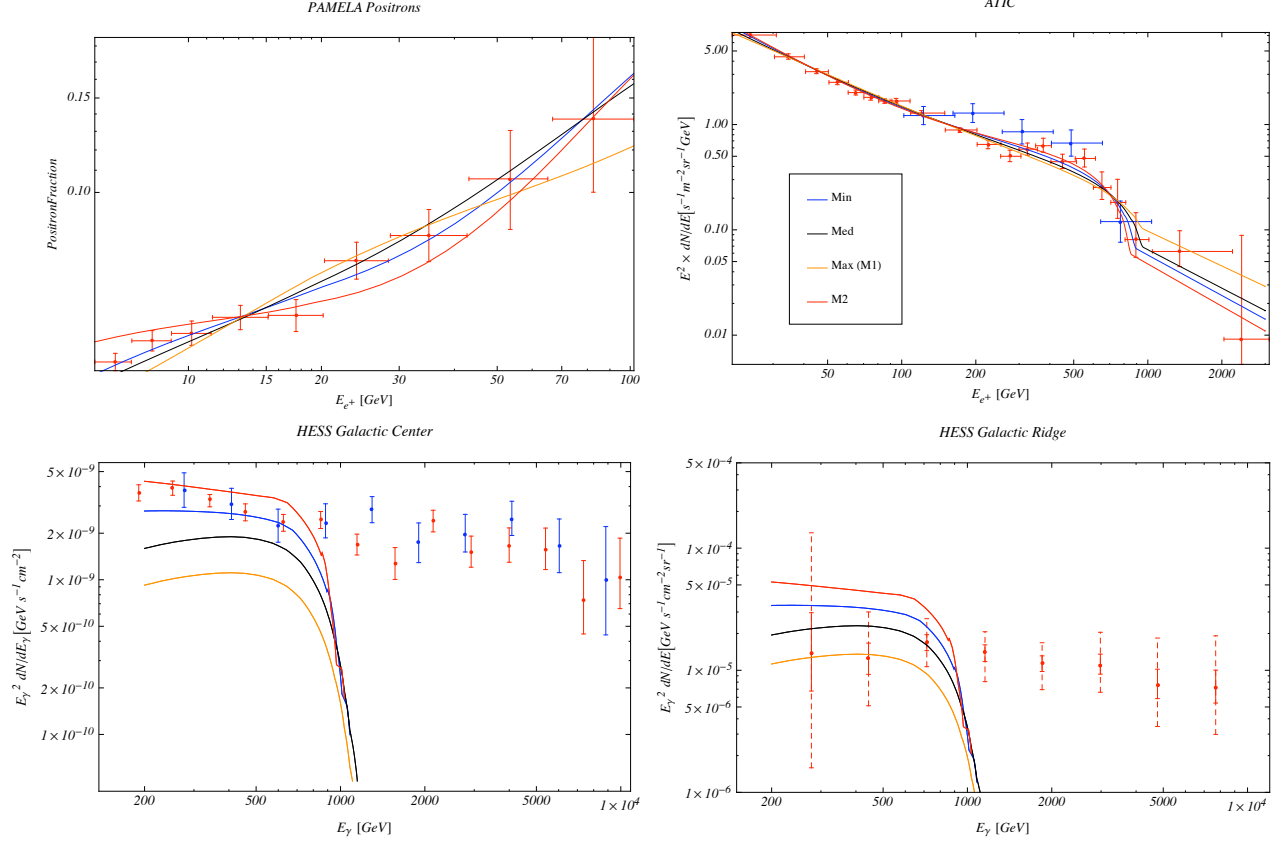


Figure 14: Plots for different propagation models, with $m_\phi = 200$ MeV. The best fit parameters used are given in Table 7. The neutrino spectrum is not shown since none are produced due to kinematics. The predictions for photons are shown in the last two plots overlaid with the HESS measurements. Around each bin of the HESS data, we indicate the 1σ (solid) and 3σ (dashed) error bar.

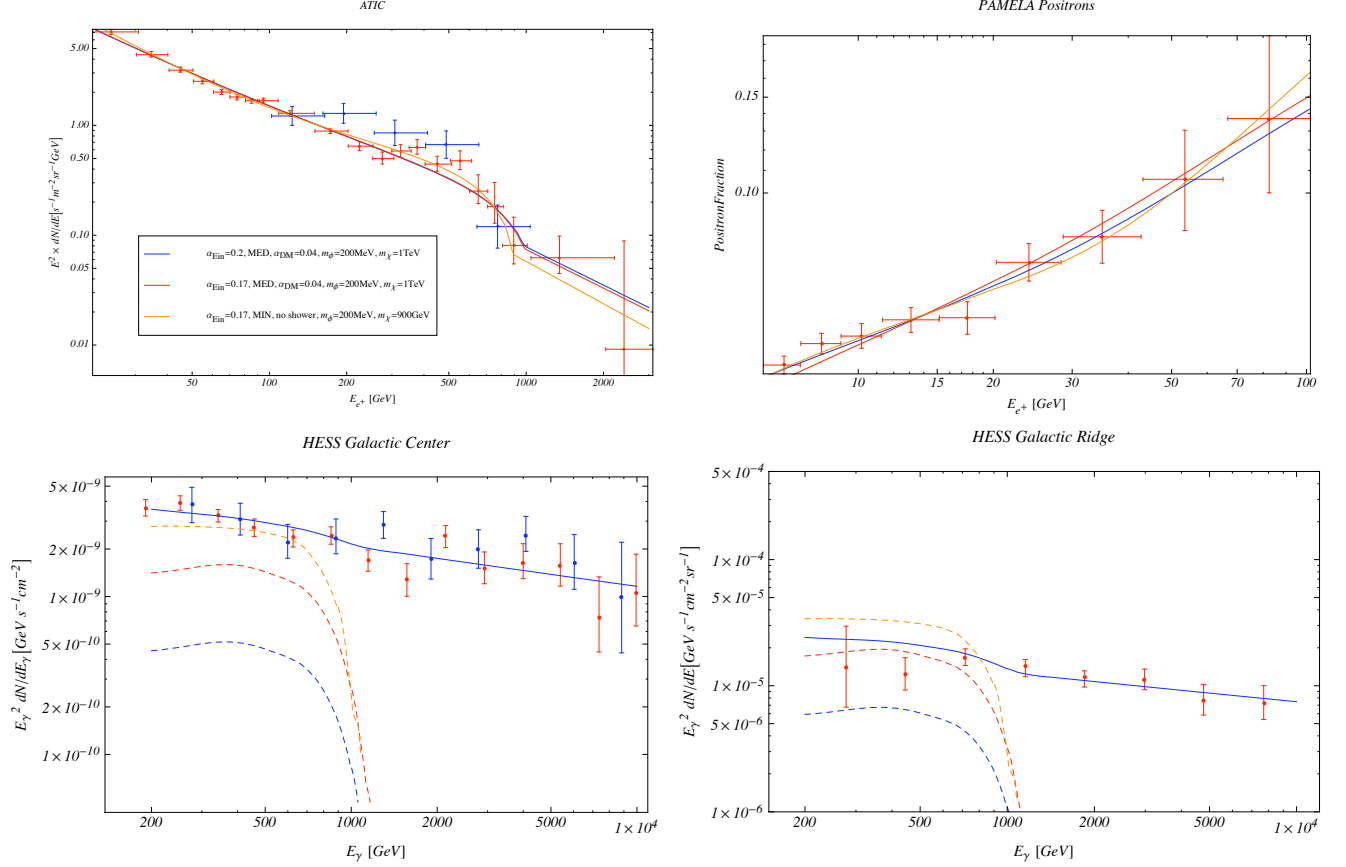


Figure 15: The best fit including HESS/PAMELA/ATIC/PPB-BETS is plotted in blue(lower blue curve is signal only in the HESS plots), which is for $m_\chi = 1 \text{ TeV}$, $m_\phi = 200 \text{ MeV}$, $\langle\sigma v\rangle = 8.2 \cdot 10^{-24} \text{ cm}^3/\text{s}$ and $\alpha_{DM} = .04$, for an Einasto profile with $\alpha = .2$ and the med propagation parameters. The best fit including PAMELA/ATIC/PPB-BETS without HESS is plotted in orange. The parameters are $m_\chi = 900 \text{ GeV}$, $m_\phi = 200 \text{ MeV}$, $\langle\sigma v\rangle = 1.1 \cdot 10^{-23} \text{ cm}^3/\text{s}$, with no parton shower, an Einasto density profile with $\alpha = .17$ and MIN propagation.

ters. Additionally, for comparison, Figure 15 shows the same parameters except we change the DM profile to Einasto $\alpha = 0.17$. Furthermore, we show in the figure how HESS alters this fit by giving the best fit case where only PAMELA and ATIC/PPB-BETS are included in the χ^2 . This corresponds to a best fit point of $m_\chi = 900 \text{ GeV}$, $m_\phi = 200 \text{ MeV}$, $\langle\sigma v\rangle = 1.1 \cdot 10^{-23} \text{ cm}^3/\text{s}$, with no parton shower, an Einasto density profile with $\alpha = 0.17$ and MIN propagation parameters. As we can see, one can find a fit for annihilating background that *includes* a photon background for HESS and satisfies the data. Still, for a good fit, the DM profile is required to be less cuspy than the preferred profile of $\alpha = 0.17$. We can also quantify a suppression factor for an Einasto profile with $\alpha = 0.17$, that could come in principle from several sources, so that the effective \bar{J} is as good as our best fit point. For

$m_\phi = 200$ MeV one needs a suppression factor of 3-4, for $m_\phi = 500$ MeV we need a factor of 4, while for 1.2 GeV we need a larger suppression of $\mathcal{O}(10)$.

A recent paper [16] investigated the case of DM annihilating through a light ϕ and then into leptons. Their claim was that models of this type that satisfied PAMELA/ATIC with standard DM density profiles were ruled out unless an order of magnitude local boost factor was included. Their most stringent bounds come from examining Sgr A*, in radio frequencies similar to [15]. Unfortunately, such a constraint is highly sensitive to knowledge of the DM density profile at distances much below 100 pc which is beyond the resolution limit of current simulations. Nonetheless, if one takes the bound at face value we find that their band that agrees with the PAMELA measurement is different than ours, and we can fit both PAMELA and their radio bound. In the region of high energy gammas this constraint is not more significant than the HESS GC one. The authors also consider bounds from the Sagittarius dwarf galaxy. Since the Sagittarius dwarf galaxy is being tidally disrupted by the Milky Way it is dubious to trust bounds coming from this alone. We have checked for one of the most studied dwarf galaxies, Draco (that is not too close to our Galaxy to be tidally disrupted), that the bounds are easily satisfied by at least an order of magnitude. As discussed, the most significant bound we find arises from the study of the GR region, and as shown in Figure 15 they can be satisfied.

While there exist points in parameter space that can satisfy all experimental constraints, this does not mean that generically there is no tension between DM annihilation models of this type and the experimental results. As we can see from Section 4, in many regions of parameter space the HESS experiment would completely rule out models from the GR data. This is due to the fact that the HESS experiment in both the GC and the GR, records data that has a best fit to a power law. Once one includes DM annihilating in the energy range that HESS studies, it automatically introduces a non-power law shape on top of the background. Since the PAMELA experiment currently studies energies less than the photon energies recorded by HESS, there is no tension between these experiments. However, the inclusion of ATIC/PPB-BETS experiments, automatically signal a mass scale which creates the tension. We demonstrate this in Figure 16 where we separate our χ^2 function into χ^2_{HESS} and $\chi^2_{\text{ATIC/PAMELA}}$ and plot two dimensional contours of χ^2 for each, in the space of m_χ and $\langle\sigma v\rangle$. As we can see from Figure 16 the best fit for χ^2 taking into account PAMELA/ATIC/PPB-BETS alone prefers a lower mass scale and higher cross-sections, while HESS prefers a low cross-sections and potentially higher masses in order to preserve its pure power law background.

This generic tension could mean several things. First, the excesses in PAMELA and ATIC/PPB-BETS may simply be caused by astrophysics. Pulsars for instance could explain the leptonic excesses without necessarily introducing a large component of high energy gamma rays at the center of our galaxy. Second, it could be a red herring, and as we have demonstrated, models of this type do have points in parameter space that could account for the experimental data. Another way to avoid the tension would be to investigate models of decaying DM [7] instead of annihilating DM since the amount of photons at the center of the galaxy would then scale like ρ instead of ρ^2 . While these are all possible interpretations,

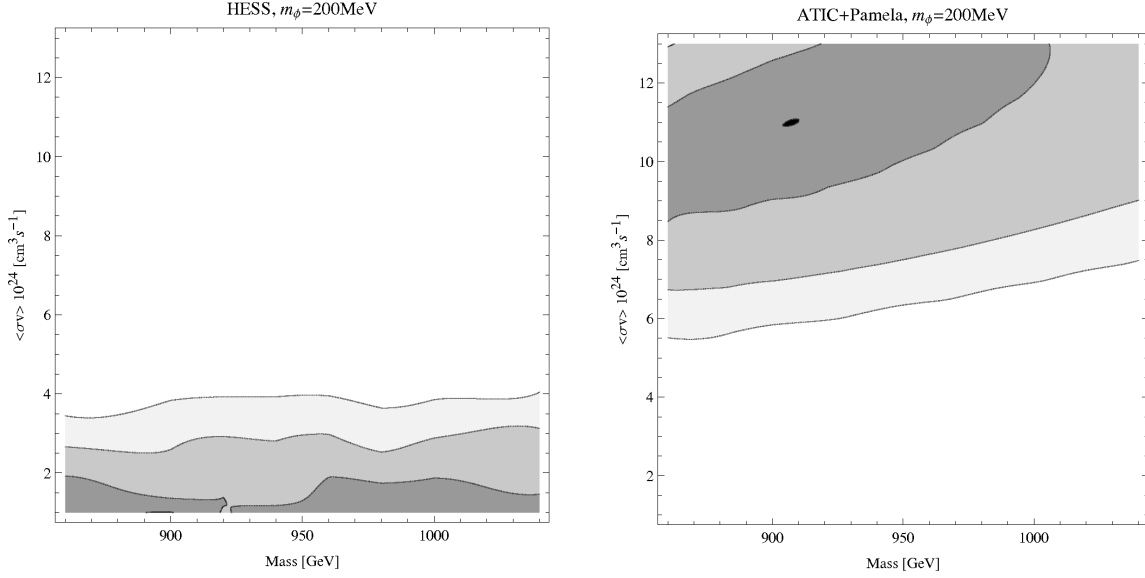


Figure 16: Comparison between the χ_{HESS}^2 and $\chi_{\text{ATIC/PAMELA}}^2$ for $m_\phi = 200$ MeV as a function of mass and cross-section.

we wish to point out another.

The starting point of current DM investigations is to automatically assume all the recent excesses reported by experiments, and work under the assumption that there is/will be no conflicting data. For instance in the case of the ATIC/PPB-BETS experiments the excesses that are shown conflict with the existing EC [78] data. It has been pointed out in the past that EC was based on a much smaller detector area and thus could be more prone to systematic errors. This could be the cause of the apparent discrepancy between the ATIC/PPB-BETS and EC data. Still, it is curious nonetheless that ATIC/PPB-BETS and HESS are the experiments that seem to have a tension if the picture of annihilating DM is true. One possibility could be that the anomaly observed by ATIC disappears in the future, or that the excess they see is unrelated to DM but rather to astrophysics (e.g. cooling). In this case a model would only need to satisfy the PAMELA experiment and the mass scale could be much lower in principle.

In Figure 17 we demonstrate the consequences of assuming only the PAMELA experiment and we fit to the electron flux below 100 GeV. The fact that this is a viable option is not immediately clear without calculating the results for the other experiments. Indeed, if one lowers the mass scale, there are several potential difficulties that need to be confronted. One needs to make sure that no feature is introduced in the electron flux that would have been seen thus far. At lower energies, even though one can avoid the bounds from the HESS GR data, in principle one could now be in danger of over-populating the low energy photons for the EGRET experiment. As we show in Figure 17 for the case of $m_\chi \sim 250$ GeV, $m_\phi = 200$ MeV and $\langle\sigma v\rangle = 9.65 \cdot 10^{-25} \text{ cm}^3/\text{s}$, with an Einasto density profile for $\alpha = 0.17$ and MED

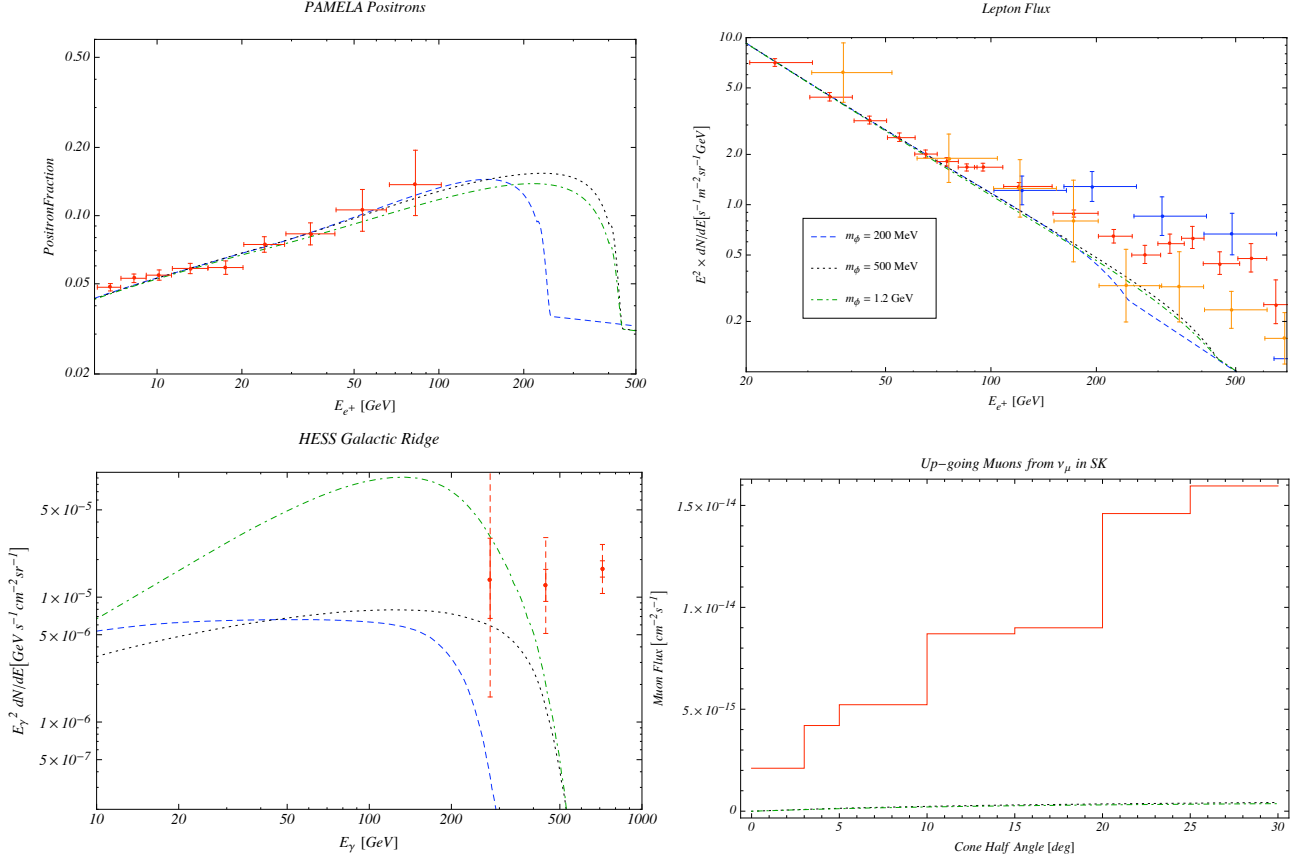


Figure 17: We plot the best fit for $m_\phi = 0.2, 0.5, 1.2$ GeV excluding the data from ATIC/PPB-BETS above 100 GeV. The best fit point corresponds to $m_\chi = 250$ GeV, $m_\phi = 200$ MeV and $\langle\sigma v\rangle = 9.65 \cdot 10^{-25} \text{ cm}^3/\text{s}$, with an Einasto density profile for $\alpha = 0.17$ and MED propagation.

propagation, one can satisfy all experimental constraints easily with $\chi^2/\text{dof} \sim 1$. This is an incredibly interesting prospect as it opens up possible new avenues for model building and additionally provides even *more* testable predictions. By lowering the mass scale the high energy photons are now completely within reach of the FERMI experiment [17] and furthermore a nontrivial turnover in the positron fraction measured by PAMELA could be observed. In Figure 17 we plot the photon flux expected from the high energy photons observable by FERMI when looking at the GC. This is well within the sensitivity range of the experiment, and it is an open question whether or not the high energy photons are observable compared to the ICS contribution. We postpone this for future work [79].

As we have stated, there are several possibilities for explaining the excesses: annihilating DM for low or high m_χ , decaying DM, Astrophysics/pulsars, some unknown idea or combination thereof. Whatever it turns out to be, we are in a golden age of experiments and it's useful to review what are the most important experimental results/possible measurements

that could be done to sort out potential DM candidates.

- **PAMELA:** Future measurements of the positron flux can tell us whether or not the fraction continues to increase throughout its mass range and has bearing on whether or not DM is heavy or not.
- **FERMI:** Has the ability to confirm or reject the ATIC/PPB-BETS excesses by measuring the electron flux. Additionally if the DM is light FERMI will be in the exact range needed to study it's properties.
- **ATIC:** The release of ATIC-4 data will offer better statistics and will allow for a better comparison to HESS's recent release of the lepton flux at the high end of ATIC's reach [80].
- **HESS:** Has already bounded high scale annihilating DM by studying the GR with only a relatively short amount of data taking. In principle by collecting more data, it could rule out beyond a shadow of the doubt high scale annihilating DM.

These possible results combined with other experiments should allow us within the next few years to confirm or rule out many possibilities for DM. As it stands now, we have demonstrated that the particle physics module we have implemented can account for existing data. In the near future we will hopefully be able to further pin down or rule out the properties of models that have the features we examined.

Note Added: While this paper was in preparation we learned of a similar work in progress by Jeremy Mardon, Yasunori Nomura, Daniel Stolarski, and Jesse Thaler [81].

Acknowledgments

We would like to thank Nima Arkani-Hamed, Kfir Blum, Marco Cirelli, Boaz Katz, Michael Kuhlen, Gilad Perez, Alessandro Strumia, Eli Waxman and Neal Weiner for useful discussions. PM and TV are supported in part by DOE grant DE-FG02-90ER40542. MP is supported in part by NSF grant PH0503584.

A The Leaky Box Approximation

In this Appendix we describe the leaky box approximation which is used to estimate the background for the positron flux for energies $\lesssim 100$ GeV. This model is essentially a simplified version of that described in section 3.2.1. Its value lies in its minimal set of assumptions, allowing one to examine the data with as few extra theoretical inputs as possible.

The confinement time of charged particles in the Galactic disk is enhanced due to galactic magnetic fields and is of order $t_{\text{esc}} \sim 10^7 (E/\text{GeV})^{-0.6}$ yr. On the other hand, the cooling

time due to ICS and synchrotron radiation is of order $t_{cool} \sim 2 \times 10^8 (E/\text{GeV})^{-1}$ yr. Thus for energies below ~ 100 GeV, the particles either reach the Earth or escape the Galaxy before losing energy and therefore cooling can be neglected. For the background computation below, we assume this is the case.

The leaky box approximation is a simplified diffusion model which takes into account the confinement of charged particles. The model assumes a free homogeneous diffusion of charged particles within the galactic disk. At the galactic boundaries, particles are either reflected or escape with finite energy-dependent probability. In its simplest form, the only independent parameter is the mean density of matter, λ_{esc} , traversed by the charged particle before escaping. One has $\lambda_{esc} = \rho_{ISM} \beta c t_{esc}$ where ρ_{ISM} is the average interstellar matter (ISM) density in the galaxy (not to be confused with the density in the galactic disk) and t_{esc} is the escaping time. Under the assumption that λ_{esc} depends only on the rigidity, $\mathcal{R} = pc/Ze$ of the charged particle, λ_{esc} is extracted by measuring secondary to primary ratios. The B/C measurements from the HEAO-3 experiment [48] and other balloon experiments (the most recent being ATIC-2 [49]), provide the most stringent constraint. For particles with rigidity $\mathcal{R} > 4.5$ GV one finds [82, 83],

$$\lambda_{esc} = 23.8 \beta \left(\frac{\mathcal{R}}{\text{GV}} \right)^{-\delta} \text{ g cm}^{-2}. \quad (\text{A.1})$$

with $\delta \sim 0.6$. As discussed in section 3.2.1, other propagation models allow variations in δ between $\delta \sim .45 - .85$. To be conservative we consider these values here.

In the absence of cooling effects and losses due to collisions, the master transport equation at equilibrium for a stable nuclei takes a simple form,

$$\frac{n_i(E_i)}{\tau_i(E_i)} = Q_i^{\text{prim}}(E_i) + Q_i^{\text{sec}}(E_i). \quad (\text{A.2})$$

Here $Q_i^{\text{prim(sec)}}$ is the primary (secondary) source term for a particle of type i with,

$$Q_i^{\text{sec}}(E_i) = \frac{\beta c \rho_{ISM}}{m} \sum_j \int dE_j n_j(E_j) \frac{d\sigma(E_j \rightarrow E_i)}{dE_i}. \quad (\text{A.3})$$

n_i is the number density per unit energy which is related to the flux through $\Phi_i = (v_i/4\pi)n_i$. For positrons, where primary sources are absent, the first term on the RHS of (A.2) vanishes and one finds,

$$n_{e^+}(E) = Q_{e^+}^{\text{sec}}(E) t_{esc}(E) = \frac{\lambda_{esc}}{m} \langle n_p \sigma_p \rangle, \quad (\text{A.4})$$

where $Q_{e^+}^{\text{sec}}$ is the secondary source of positrons generated at the point of interaction, and $\langle n_p \sigma_p \rangle \equiv \sum_j \int dE_j n_j(E_j) \frac{d\sigma}{dE_i}(E_j \rightarrow E_i)$. For positrons spallation occurs through interactions of protons and α particles with ISM. Since to a good approximation σ_p does not depend

on energy (other than a sharp kinematical cutoff [84]), a prediction of this theory is that the ratio of positron-to-proton flux is proportional to the escape time,

$$\frac{\Phi_{e^+}}{\Phi_p} \propto \lambda_{\text{esc}} \sim \left(\frac{\mathcal{R}_{e^+}}{\text{GV}} \right)^{-\delta}. \quad (\text{A.5})$$

The positron injection spectrum, $Q_{e^+}^{\text{sec}}$, can be computed using the measurements of the protons flux which leads to the fit given in Eq. (4.4) and the table below it. The differential cross-section for the spallation was derived in [84] and the theoretical uncertainties were analyzed in [28]. In light of these uncertainties, we give a rough estimate for the positron source (taking for positrons $e\mathcal{R} \simeq E$),

$$Q_{e^+} \simeq 4 \times 10^{-27} \left(\frac{E_{e^+}}{\text{GeV}} \right)^{-2.84 \pm 0.02} \text{ cm}^{-3} \text{ s}^{-1} \text{ sr}^{-1} \text{ GeV}^{-1}, \quad (\text{A.6})$$

were we took $\rho_{\text{ISM}}/m = 0.9 \text{ cm}^{-3}$. Using eq. (A.1), the results, Eq. (3.15) follows. We stress that the coefficient for the positron flux may suffer from corrections of order 100%.

References

- [1] O. Adriani *et al.*, “Observation of an anomalous positron abundance in the cosmic radiation,” arXiv:0810.4995 [astro-ph].
- [2] S. Torii *et al.*, arXiv:0809.0760 [astro-ph].
- [3] J. Chang et al., in Proc. of the 29th International Cosmic Ray Conference (ICRC 2005), (Tata Institute of Fundamental Research, Mumbai, 2005), vol. 3, p. 1.
- [4] P. D. Serpico, arXiv:0810.4846 [hep-ph], D. Hooper, P. Blasi and P. D. Serpico, JCAP **0901**, 025 (2009) [arXiv:0810.1527 [astro-ph]], H. Yuksel, M. D. Kistler and T. Stanev, arXiv:0810.2784 [astro-ph], S. Profumo, arXiv:0812.4457 [astro-ph].
- [5] N. Arkani-Hamed, D. P. Finkbeiner, T. Slatyer and N. Weiner, arXiv:0810.0713 [hep-ph].
- [6] Y. Nomura and J. Thaler, arXiv:0810.5397 [hep-ph]. R. Harnik and G. D. Kribs, arXiv:0810.5557 [hep-ph]. P. J. Fox and E. Poppitz, arXiv:0811.0399 [hep-ph]. E. Ponton and L. Randall, arXiv:0811.1029 [hep-ph]. K. M. Zurek, arXiv:0811.4429 [hep-ph]. P. Grajek, G. Kane, D. Phalen, A. Pierce and S. Watson, arXiv:0812.4555 [hep-ph]. P. Grajek, G. Kane, D. J. Phalen, A. Pierce and S. Watson, arXiv:0807.1508 [hep-ph]. M. Pospelov and A. Ritz, arXiv:0810.1502 [hep-ph]. M. Fairbairn and J. Zupan, arXiv:0810.4147 [hep-ph]. R. Allahverdi, B. Dutta, K. Richardson-McDaniel and Y. Santoso, arXiv:0812.2196 [hep-ph]. E. J. Chun and J. C. Park, arXiv:0812.0308 [hep-ph]. A. E. Nelson and C. Spitzer, arXiv:0810.5167 [hep-ph]. J. H. Huh, J. E. Kim

- and B. Kyae, arXiv:0809.2601 [hep-ph]. L. Bergstrom, T. Bringmann and J. Edsjo, arXiv:0808.3725 [astro-ph]. C. R. Chen, F. Takahashi and T. T. Yanagida, arXiv:0811.0477 [hep-ph], S. Baek and P. Ko, arXiv:0811.1646 [hep-ph].
- [7] P. f. Yin, Q. Yuan, J. Liu, J. Zhang, X. j. Bi and S. h. Zhu, arXiv:0811.0176 [hep-ph], A. Ibarra and D. Tran, arXiv:0811.1555 [hep-ph], C. R. Chen, M. M. Nojiri, F. Takahashi and T. T. Yanagida, arXiv:0811.3357 [astro-ph]. E. Nardi, F. Sannino and A. Strumia, arXiv:0811.4153 [hep-ph].
 - [8] O. Adriani *et al.*, “A new measurement of the antiproton-to-proton flux ratio up to 100 GeV in the cosmic radiation,” arXiv:0810.4994 [astro-ph].
 - [9] J. Hisano, S. Matsumoto, M. M. Nojiri and O. Saito, “Non-perturbative effect on dark matter annihilation and gamma ray signature from galactic center,” Phys. Rev. D **71**, 063528 (2005) [arXiv:hep-ph/0412403].
 - [10] M. Ibe, H. Murayama and T. T. Yanagida, arXiv:0812.0072 [hep-ph].
 - [11] J. D. March-Russell and S. M. West, arXiv:0812.0559 [astro-ph], W. Shepherd, T. M. P. Tait and G. Zaharijas, arXiv:0901.2125 [hep-ph].
 - [12] J. Diemand, M. Kuhlen, P. Madau, M. Zemp, B. Moore, D. Potter and J. Stadel, arXiv:0805.1244 [astro-ph]. V. Springel *et al.*, arXiv:0809.0894 [astro-ph].
 - [13] A. Birkedal, K. Matchev and M. Perelstein, Phys. Rev. D **70**, 077701 (2004) [arXiv:hep-ph/0403004].
 - [14] N. F. Bell and T. D. Jacques, arXiv:0811.0821 [astro-ph].
 - [15] G. Bertone, M. Cirelli, A. Strumia and M. Taoso, arXiv:0811.3744 [astro-ph].
 - [16] L. Bergstrom, G. Bertone, T. Bringmann, J. Edsjo and M. Taoso, arXiv:0812.3895 [astro-ph].
 - [17] <http://fermi.gsfc.nasa.gov/> E. A. Baltz *et al.*, JCAP **0807**, 013 (2008) [arXiv:0806.2911 [astro-ph]].
 - [18] B. J. Teegarden *et al.*, Astrophys. J. **621**, 296 (2005) [arXiv:astro-ph/0410354].
 - [19] R. Bernabei *et al.* [DAMA Collaboration], Eur. Phys. J. C **56**, 333 (2008) [arXiv:0804.2741 [astro-ph]].
 - [20] B. Aubert *et al.* [BABAR Collaboration], Phys. Rev. D **76**, 092005 (2007) [Erratum-ibid. D **77**, 119902 (2008)] [arXiv:0708.2461 [hep-ex]], B. Aubert *et al.* [BABAR Collaboration], Phys. Rev. D **70**, 072004 (2004) [arXiv:hep-ex/0408078], R. R. Akhmetshin *et al.*, Phys. Lett. B **551**, 27 (2003) [arXiv:hep-ex/0211004], M. N. Achasov *et al.*, Phys. Lett. B **462**, 365 (1999) [arXiv:hep-ex/9910001], S. I. Dolinsky *et al.*, Phys. Rept. **202**,

- 99 (1991), S. I. Dolinsky *et al.*, Phys. Lett. B **174** (1986) 453, V. P. Druzhinin *et al.*, IYF-84-93, S. I. Eidelman [CMD-2 and SND Collaborations], Nucl. Phys. Proc. Suppl. **144**, 223 (2005) [Nucl. Phys. Proc. Suppl. **169**, 265 (2007)].
- [21] T. Sjostrand, S. Mrenna and P. Skands, JHEP **0605**, 026 (2006) [arXiv:hep-ph/0603175].
 - [22] F. Maltoni and T. Stelzer, JHEP **0302**, 027 (2003) [arXiv:hep-ph/0208156].
 - [23] P. Meade and M. Reece, arXiv:hep-ph/0703031.
 - [24] T. Gleisberg, S. Hoche, F. Krauss, M. Schoenherr, S. Schumann, F. Siegert and J. Winter, arXiv:0811.4622 [hep-ph].
 - [25] L. Bergstrom, T. Bringmann, M. Eriksson and M. Gustafsson, Phys. Rev. Lett. **95**, 241301 (2005) [arXiv:hep-ph/0507229]. T. Bringmann, L. Bergstrom and J. Edsjo, JHEP **0801**, 049 (2008) [arXiv:0710.3169 [hep-ph]].
 - [26] M. Cirelli, R. Franceschini and A. Strumia, Nucl. Phys. B **800**, 204 (2008) [arXiv:0802.3378 [hep-ph]]. M. Cirelli and A. Strumia, arXiv:0808.3867 [astro-ph].
 - [27] I. V. Moskalenko and A. W. Strong, Phys. Rev. D **60**, 063003 (1999) [arXiv:astro-ph/9905283].
 - [28] T. Delahaye, F. Donato, N. Fornengo, J. Lavalle, R. Lineros, P. Salati and R. Taillet, arXiv:0809.5268 [astro-ph].
 - [29] T. Delahaye, R. Lineros, F. Donato, N. Fornengo and P. Salati, Phys. Rev. D **77**, 063527 (2008) [arXiv:0712.2312 [astro-ph]].
 - [30] J. F. Navarro, C. S. Frenk and S. D. M. White, Astrophys. J. **462**, 563 (1996) [arXiv:astro-ph/9508025].
 - [31] L. Hernquist, Astrophys. J. **356**, 359 (1990). H. Zhao, Mon. Not. Roy. Astron. Soc. **278**, 488 (1996) [arXiv:astro-ph/9509122].
 - [32] J. Diemand, B. Moore and J. Stadel, Mon. Not. Roy. Astron. Soc. **353**, 624 (2004) [arXiv:astro-ph/0402267].
 - [33] J. Diemand, M. Zemp, B. Moore, J. Stadel and M. Carollo, Mon. Not. Roy. Astron. Soc. **364**, 665 (2005) [arXiv:astro-ph/0504215].
 - [34] J. N. Bahcall and R. M. Soneira, Astrophys. J. Suppl. **44**, 73 (1980).
 - [35] J. F. Navarro *et al.*, Mon. Not. Roy. Astron. Soc. **349**, 1039 (2004) [arXiv:astro-ph/0311231].
 - [36] Einasto J., 1965, Trudy Inst. Astroz. Alma-Ata, 51, 87

- [37] D. Merritt, J. F. Navarro, A. Ludlow and A. Jenkins, *Astrophys. J.* **624**, L85 (2005) [arXiv:astro-ph/0502515].
- [38] J. F. Navarro *et al.*, arXiv:0810.1522 [astro-ph].
- [39] M. Kuhlen, J. Diemand, P. Madau and M. Zemp, *J. Phys. Conf. Ser.* **125**, 012008 (2008) [arXiv:0810.3614 [astro-ph]].
- [40] J. Stadel *et al.*, arXiv:0808.2981 [astro-ph].
- [41] M. Kamionkowski and A. Kinkhabwala, *Phys. Rev. D* **57**, 3256 (1998) [arXiv:hep-ph/9710337].
- [42] C. Amsler *et al.* [Particle Data Group], *Phys. Lett. B* **667**, 1 (2008).
- [43] M. Kamionkowski and S. M. Koushiappas, *Phys. Rev. D* **77**, 103509 (2008) [arXiv:0801.3269 [astro-ph]].
- [44] M. Zemp *et al.*, arXiv:0812.2033 [astro-ph].
- [45] A. Barrau, P. Salati, G. Servant, F. Donato, J. Grain, D. Maurin and R. Taillet, *Phys. Rev. D* **72**, 063507 (2005) [arXiv:astro-ph/0506389].
- [46] V. L. Ginzburg and V. S. Ptuskin, *Rev. Mod. Phys.* **48** (1976) 161 [Erratum-ibid. **48** (1976) 675].
- [47] For a review see, A. W. Strong, I. V. Moskalenko and V. S. Ptuskin, *Ann. Rev. Nucl. Part. Sci.* **57**, 285 (2007) [arXiv:astro-ph/0701517].
- [48] J. J. Engelmann *et al.*, *Astronomy and Astrophysics*, **233** 96 (1990)
- [49] A. D. Panov *et al.*, arXiv:0707.4415 [astro-ph].
- [50] D. Maurin, F. Donato, R. Taillet and P. Salati, *Astrophys. J.* **555**, 585 (2001) [arXiv:astro-ph/0101231].
- [51] F. Donato, N. Fornengo, D. Maurin and P. Salati, *Phys. Rev. D* **69**, 063501 (2004) [arXiv:astro-ph/0306207].
- [52] A. M. Hillas, *J. Phys. G* **31**, R95 (2005).
- [53] E. A. Baltz and J. Edsjo, *Phys. Rev. D* **59**, 023511 (1999) [arXiv:astro-ph/9808243].
- [54] S. W. Barwick *et al.*, *Astrophys. J.* **498**, 779 (1998) [arXiv:astro-ph/9712324].
- [55] M. Boezio, talk at the "LHC and Dark Matter Workshop", Michigan Center for Theoretical Physics, 2009.

- [56] J. Hisano, S. Matsumoto, O. Saito and M. Senami, Phys. Rev. D **73** (2006) 055004 [arXiv:hep-ph/0511118].
- [57] L. C. Tan and L. K. Ng, J. Phys. G **9** (1983) 1289.
- [58] F. Donato, D. Maurin, P. Salati, A. Barrau, G. Boudoul and R. Taillet, Astrophys. J. **563**, 172 (2001) [arXiv:astro-ph/0103150].
- [59] Y. Shikaze *et al.*, Astropart. Phys. **28**, 154 (2007) [arXiv:astro-ph/0611388].
- [60] T. Sanuki *et al.*, Astrophys. J. **545**, 1135 (2000) [arXiv:astro-ph/0002481]. S. Haino *et al.*, Phys. Lett. B **594**, 35 (2004) [arXiv:astro-ph/0403704].
- [61] M. Aguilar *et al.* [AMS-01 Collaboration], Phys. Lett. B **646**, 145 (2007) [arXiv:astro-ph/0703154]. J. Alcaraz *et al.* [AMS Collaboration], Phys. Lett. B **490**, 27 (2000). J. Alcaraz *et al.* [AMS Collaboration], Phys. Lett. B **472**, 215 (2000) [arXiv:hep-ex/0002049].
- [62] F. Donato, D. Maurin, P. Brun, T. Delahaye and P. Salati, arXiv:0810.5292 [astro-ph].
- [63] L.J. Gleeson and W.I. Axford, ApJ 149 (1967) L115 and L.J. Gleeson and W.I. Axford, ApJ 154 (1968) 1011.
- [64] N. W. Evans, F. Ferrer and S. Sarkar, Phys. Rev. D **69**, 123501 (2004) [arXiv:astro-ph/0311145].
- [65] M. Kuhlen, J. Diemand and P. Madau, arXiv:0805.4416 [astro-ph]. J. Diemand, M. Kuhlen and P. Madau, Astrophys. J. **657**, 262 (2007) [arXiv:astro-ph/0611370].
- [66] F. Aharonian *et al.* [H.E.S.S. Collaboration], Phys. Rev. Lett. **97**, 221102 (2006) [Erratum-ibid. **97**, 249901 (2006)] [arXiv:astro-ph/0610509].
- [67] F. Aharonian *et al.* [H.E.S.S. Collaboration], Nature **439**, 695 (2006) [arXiv:astro-ph/0603021].
- [68] S. Ritz and D. Seckel, Nucl. Phys. B **304**, 877 (1988).
- [69] G. Jungman, M. Kamionkowski and K. Griest, Phys. Rept. **267**, 195 (1996) [arXiv:hep-ph/9506380].
- [70] H. Yuksel, S. Horiuchi, J. F. Beacom and S. Ando, Phys. Rev. D **76** (2007) 123506 [arXiv:0707.0196 [astro-ph]].
- [71] J. Hisano, M. Kawasaki, K. Kohri and K. Nakayama, arXiv:0812.0219 [hep-ph]. J. Liu, P. f. Yin and S. h. Zhu, arXiv:0812.0964 [astro-ph].
- [72] C. Delaunay, P. J. Fox and G. Perez, arXiv:0812.3331 [hep-ph].
- [73] S. Desai *et al.* [Super-Kamiokande Collaboration], Phys. Rev. D **70**, 083523 (2004) [Erratum-ibid. D **70**, 109901 (2004)] [arXiv:hep-ex/0404025].

- [74] M. Cirelli, M. Kadastik, M. Raidal and A. Strumia, arXiv:0809.2409 [hep-ph].
- [75] A. Putze, L. Derome, D. Maurin, L. Perotto and R. Taillet, arXiv:0808.2437 [astro-ph].
- [76] I. V. Moskalenko, A. W. Strong, J. F. Ormes and M. S. Potgieter, *Astrophys. J.* **565**, 280 (2002) [arXiv:astro-ph/0106567].
- [77] A. W. Strong and I. V. Moskalenko, *Astrophys. J.* **509**, 212 (1998) [arXiv:astro-ph/9807150].
- [78] T. Kobayashi *et al.*, “High energy cosmic-ray electrons beyond 100-GeV”, *Prepared for 26th International Cosmic Ray Conference (ICRC 99), Salt Lake City, Utah, 17-25 Aug 1999*
- [79] P. Meade, M. Papucci, T. Volansky, *work in progress*.
- [80] F. Aharonian *et al.* [H.E.S.S. Collaboration], *Phys. Rev. Lett.* **101**, 261104 (2008) [arXiv:0811.3894 [astro-ph]].
- [81] J. Mardon, Y. Nomura, D. Stolarski, and J. Thaler arXiv:0901.2926 [hep-ph].
- [82] M. Gupta and W.R. Webber 1989, *Ap. J.*, **340**, 1124 (1989).
- [83] For a recent review see, P. Blasi, arXiv:0801.4534 [astro-ph].
- [84] T. Kamae, N. Karlsson, T. Mizuno, T. Abe and T. Koi, *Astrophys. J.* **647**, 692 (2006) [arXiv:astro-ph/0605581].